CHALMERS
UNIVERSITY OF TECHNOLOGY

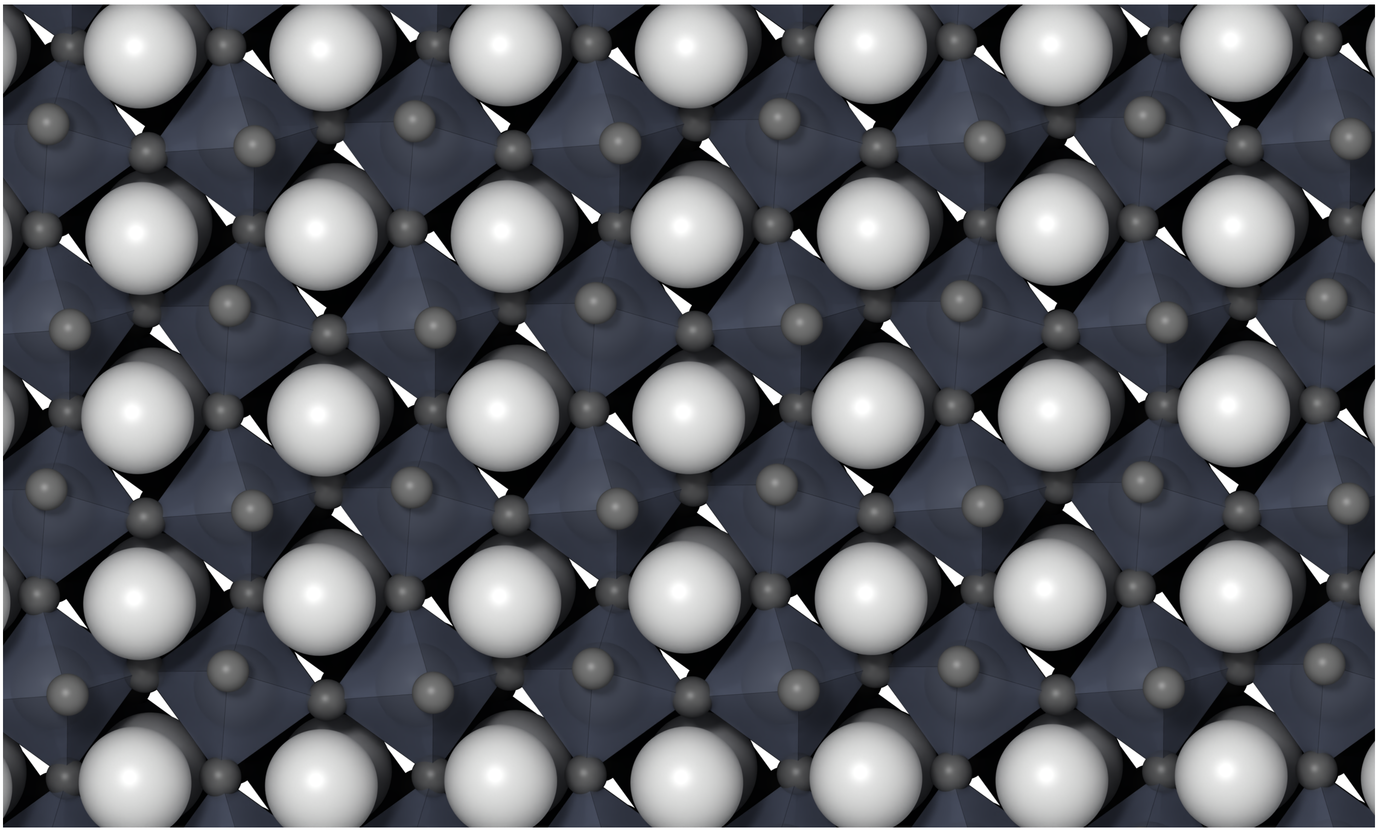

Modeling Electron-Phonon Coupling in Perovskites

Electron-phonon coupling and hybrid improper ferroelectricity via neuroevolution potential models

Master's thesis in Physics

Leo Ögren Westin

DEPARTMENT OF PHYSICS

CHALMERS UNIVERSITY OF TECHNOLOGY
Gothenburg, Sweden 2025
www.chalmers.se

MASTER'S THESIS 2025

Modeling Electron-Phonon Coupling in Perovskites

Electron-phonon coupling and hybrid improper ferroelectricity via neuroevolution potential models

Leo Ögren Westin

Department of Physics
Division of Condensed Matter and Materials Theory
Computational Materials Research group
CHALMERS UNIVERSITY OF TECHNOLOGY
Gothenburg, Sweden 2025

Modeling Electron-Phonon Coupling in Perovskites
Electron-phonon coupling and hybrid improper ferroelectricity via neuroevolution potential models
Leo Ögren Westin

Supervisor: Erik Fransson, Department of Physics
Examiner: Paul Erhart, Department of Physics

Master's Thesis 2025
Department of Physics
Division of Condensed Matter and Materials Theory
Computational Materials Research group
Chalmers University of Technology
SE-412 96 Gothenburg
Telephone +46 31 772 1000

Cover: Tilted octahedras of $Ca_3Ti_2O_7$.

Typeset in LaTeX
Printed by Chalmers Reproservice
Gothenburg, Sweden 2025

Modeling Electron-Phonon Coupling in Perovskites
Electron-phonon coupling and hybrid improper ferroelectricity via neuroevolution potential models
Leo Ögren Westin
Department of Physics
Chalmers University of Technology

Abstract

Electron-phonon coupling plays a central role in determining key material properties, such as carrier mobility and optical response. However, accurately modeling these interactions remains computationally demanding and methodologically complex. In this work, different modeling approaches to electron-phonon coupling are explored and their effectiveness is demonstrated for two prototypical perovskite systems: the halide perovskite cesium lead bromide and the oxide perovskite calcium titanate. For the oxide, the study also includes Ruddlesden–Popper phases. The objective is to understand temperature-dependent electronic properties and to develop models for band edge fluctuations and polarization behavior. For cesium lead bromide, the study focuses on the cubic phase. During molecular dynamics simulations, band gap and valence band maximum data were obtained from density functional theory calculations, and the corresponding phonon mode coordinates were extracted.

A feature-based model was developed to describe band edge fluctuations as a function of the mode coordinates. Several feature selection methods were tested, and the model was found to adequately capture fluctuations in the valence band maximum using a subset of the total phonon modes. For calcium titanate, tensorial neuroevolution potential models were trained to predict Born effective charges using density functional theory data from the perovskite structure and two Ruddlesden-Popper phases. Subsequently, predictions were made for Ruddlesden-Popper phases outside of the training set. The predicted Born effective charges were used to calculate spontaneous polarization, and the model successfully reproduced the polarization drop across the ferroelectric–paraelectric phase transition.

Keywords: electron-phonon coupling, perovskites, molecular dynamics, Born effective charge, Ruddlesden-Popper phases.

Acknowledgements

First and foremost, I would like to express my sincere gratitude to my examiner, Paul Erhart, for giving me the opportunity to work on this project. I am also deeply thankful to my supervisor, Erik Fransson, for your excellent guidance, insightful discussions, and continuous support throughout the course of this work.

I am sincerely grateful for the warm, collaborative, and inspiring environment within the division, which has made this experience both meaningful and memorable — one I will carry with me for years to come.

Finally, I would like to thank Nelly and the rest of my family for their unwavering support, encouragement, and patience — your belief in me has been invaluable.

Leo Ögren Westin, Gothenburg, June 2025

Glossary

Below is the list of acronyms that have been used throughout this thesis listed in alphabetical order:

DFPT	Density functional perturbation theory
DFT	Density functional theory
HP	Halide perovskite
MD	Molecular dynamics
NEP	Neuroevolution potential
NpT	Isothermal–isobaric ensemble
NVE	Microcanonical ensemble
NVT	Canonical ensemble
PES	Potential energy surface
RP	Ruddlesden–Popper
TNEP	Tensorial neuroevolution potential
VASP	Vienna Ab initio Simulation Package

Contents

List of Acronyms **ix**

List of Figures **xiii**

1 Introduction **1**
- 1.1 Background 1
- 1.2 Aim 1
- 1.3 Limitations 1

2 Theory **3**
- 2.1 Electronic band structure 3
- 2.2 Density functional theory 4
  - 2.2.1 Hohenberg-Kohn theorem 5
  - 2.2.2 Kohn-Sham equations 5
  - 2.2.3 Exchange-correlation approximations 6
  - 2.2.4 Self-consistency 7
  - 2.2.5 The Born-Oppenheimer approximation 7
- 2.3 Phonons 7
- 2.4 Electron-phonon coupling 10
- 2.5 Born effective charges and polarization 12
- 2.6 Molecular dynamics 13
  - 2.6.1 Sampling the canonical ensemble 14
- 2.7 Neuroevolution potential models 14

3 Perovskites **17**
- 3.1 Halide perovskites 17
- 3.2 Ruddlesden-Popper phases 18

4 Results **21**
- 4.1 Halide perovskite $CsPbBr_3$ 22
  - 4.1.1 Phase transitions and lattice parameter extraction 22
  - 4.1.2 Band gap evolution from phonon mode distortion 23
  - 4.1.3 Feature-based modeling of VBM fluctuations 27
- 4.2 Born effective charges for $CaTiO_3$ 32
  - 4.2.1 TNEP model 32
  - 4.2.2 Vibrational properties 35
- 4.3 Polarization for $Ca_3Ti_2O_7$ 37

5 Conclusion **45**

Bibliography **47**

List of Figures

2.1 Feynman diagrams for electron-phonon interactions 11

3.1 Crystal structure of halide perovskite $CsPbBr_3$ 17
3.2 Tilting of the octahedra 18
3.3 Crystal structures of RP phases 19

4.1 Phonon dispersion for the cubic structure 22
4.2 Heating and cooling simulations 23
4.3 Lattice parameter extraction 23
4.4 Potential energy surface of the M-, R- and X-point modes 24
4.5 Band gaps associated with the M-, R- and X-point modes 25
4.6 Band gaps obtained from DFT during a 20 ps MD simulation at 400 K 26
4.7 Time evolution of the mode coordinate $Q(t)$ for the harmonic X-point mode, projected from MD displacements at 400 K. 26
4.8 RMSE comparison of ARDR and RFE 28
4.9 Model performance of ARDR using 20 features against DFT data . . 28
4.10 Comparison of model performance using RFE with 10 and 40 features 29
4.11 Test set comparison of VBM model predictions using 10 features and 40 features 29
4.12 Parity plots showing predicted versus actual VBM values for models with different feature counts 30
4.13 Phonon dispersion of $CsPbBr_3$ with the most influential modes marked 31
4.14 Loss functions and parity plots for TNEP models trained with 50:50 and 95:5 train:test splits. 33
4.15 Predicted Z^*_{xx} components over time for Ca and Ti atoms during an MD simulation at constant temperature 300 K. 33
4.16 Predicted $Z^*_{\alpha\alpha}$ components over time for O atoms during an MD simulation at constant temperature 300 K. 34
4.17 Standard deviation of the average of the diagonal elements of Z^* for each atom, further averaged over all six models. 34
4.18 Variation of Z^*_{avg} with temperature for the three different atom types. 35
4.19 Average BEC of every atom type along the stacking direction of the $n = 8$ RP phase. 36
4.20 Comparison of Ca and Ti BECs in the RP $n = 8$ structure with BECs in the bulk $Pnma$ perovskite 36

4.21 Predicted polarization over time at 300 K using two different reference structures for the atomic displacements: the relaxed $I4/mmm$ structure and the non-equilibrium $Cmc2_1$ structure obtained from the first frame of the MD simulation. 37
4.22 Comparison of static and configuration-dependent BECs for all polarization components 38
4.23 Comparison of the polarization components obtained from TNEP BECs and DFT 39
4.24 Temperature dependence of lattice parameters 40
4.25 Evolution of the angles between cell vectors during heating 40
4.26 Distribution of the octahedral tilt angles as a function of temperature 41
4.27 Average displacement from the reference structure over the heating run for each atom type and Cartesian direction 42
4.28 Polarization decomposed into x, y, z components over heating. The ferroelectric to paraelectric transition is observed at ~ 1100 K. 43
4.29 Temperature dependence of the polarization magnitude 43

1

Introduction

1.1 Background

In recent years, interest in solar energy conversion has been rapidly increasing. Perovskites are promising materials for future solar cells due to their low-cost potential, defect tolerance and high efficiency [1]. However, present-day challenges have hindered the commercialization of perovskite solar cells, with one significant challenge being their poor stability under operating conditions [2, 3]. Therefore, it is of great importance to further investigate the properties of perovskite materials to achieve long-term stability.

Understanding electron-phonon interactions is crucial for identifying new materials with favorable optoelectronic properties, and models for accurately predicting their band gap is needed [4]. Accurately modeling these interactions remains a challenge due to strong anharmonicity, and it is a priori unclear how these anharmonicities impact electron-phonon interactions and the resulting material properties [5]. Thus, from a modeling point of view, electron-phonon interactions are inherently complex. This project aims to address these challenges by exploring modeling strategies across both halide and oxide perovskites, and extends further to the prediction of polarization behavior in RP-type perovskite oxides.

1.2 Aim

The aim of this thesis is to explore and evaluate the temperature-dependent electronic properties of perovskites using computational modeling. Two representative systems are studied: the halide perovskite $CsPbBr_3$ and the oxide perovskite $CaTiO_3$, including oxide RP phases.

1.3 Limitations

The limitations of this project arise from both methodological constraints and modeling assumptions. The use of density functional theory (DFT) limits system size and sampling. DFT calculations are computationally expensive and therefore restricted to systems of few atoms, which limits the ability to model large supercells. While the use of NEP-models (in this case, also TNEP-models) significantly reduces computational cost and enables larger-scale simulations, these models are still approximations. They may introduce deviations from DFT accuracy, which although

small, should still be considered when interpreting the results.
The polarization was computed from Born effective charges and atomic displacements, this does not account for domain effects or extrinsic phenomena such as defects. As a result, the predicted polarization values represent idealized behavior and may differ from those observed in real materials. Additionally, the TNEP model was trained specifically on $CaTiO_3$ and related Ruddlesden–Popper phases. Its generalizability to structurally different or more complex materials remains untested.

2

Theory

2.1 Electronic band structure

The electronic band structure describes the allowed and forbidden range of energies available to electrons. The energy ranges that are not allowed for the electrons are called band gaps, and are regarded as the energy difference between the top of the valence band and the bottom of the conduction band. The band structure provides information about the electrical properties of materials, such as whether the material is a conductor, semiconductor or an insulator. External stimuli, such as pressure or temperature change, can influence the band structure. As an example, semiconductors have a moderately low band gap, and temperature changes can make the electrons jump to the conduction band if sufficient energy is gained, this is often referred to as thermal excitation of electrons.

To determine the band structure of a solid, we need the electron energy dependence on the wave vector for various energy bands, and its order. In quantum mechanics, a particle is assumed to be described by a wavefunction $\psi(\boldsymbol{r})$ that satisfies the Schrödinger equation,

$$H\psi(\boldsymbol{r}) = E\psi(\boldsymbol{r}). \tag{2.1}$$

The Hamiltonian operator H provides information about a particular system, and is given by the sum of potential energy and kinetic energy, $H = T + V$. In crystals, the ions are arranged with a periodicity of their Bravais lattice given by lattice vectors $\mathbf{R}$. Thus, the system is described by a Hamiltonian containing a periodic potential $U(\boldsymbol{r})$ due to the periodic positioning of atoms in the crystal lattice. Solving the Schrödinger equation exactly with this periodicity considered is generally difficult. In the free electron model, where $U(\boldsymbol{r}) = 0$, the solutions are simply given by

$$\psi_{\boldsymbol{k}}(\boldsymbol{r}) = e^{i\boldsymbol{k}\cdot\boldsymbol{r}},$$

where $\boldsymbol{k}$ is the wavevector. However, in a real crystal the potential $U(\boldsymbol{r})$ must have the same periodicity as the lattice,

$$U(\boldsymbol{r} + \boldsymbol{R}) = U(\boldsymbol{r}),$$

for any lattice vector $\boldsymbol{R}$ and the wavefunctions must adapt accordingly. Bloch's theorem addresses this and states that the solutions of the Schrödinger equation with a periodic potential are given by the *Bloch functions*:

$$\psi_{n\boldsymbol{k}}(\boldsymbol{r}) = u_{n\boldsymbol{k}}(\boldsymbol{r})\, e^{i\boldsymbol{k}\cdot\boldsymbol{r}}.$$

The solutions are given by plane waves modulated by the factor $u_{n\boldsymbol{k}}(\boldsymbol{r})$, having the same periodicity as the lattice [6].

The wavevector $\boldsymbol{k}$ is a key parameter in Bloch's theorem, as it is directly related to the crystal momentum of the electron, and for a given $\boldsymbol{k}$ there are several solutions to the Schrödinger equation yielding different energy eigenvalues. The electronic energy becomes a continuous function of the wave vector, and a collection of these functions is what eventually builds the band structure of the material. Since the wavevector plays such a crucial role in describing electron states, it is natural to consider the space in which these wavevectors exist, the reciprocal space. In a Bravais lattice, the local environment appears identical from any equivalent lattice point. However, to analyze electron behavior or lattice vibrations, which is characterized by waves, it is often more convenient to consider the reciprocal space. The reciprocal space is basically a Fourier transform of the Bravais lattice, mapping real-space periodicity to points in reciprocal space.

Consider a Bravais lattice defined by the translation vectors $\mathbf{a}_1, \mathbf{a}_2, \mathbf{a}_3$, the reciprocal lattice are given by:

$$\begin{aligned}
\mathbf{b}_1 &= \frac{2\pi}{V}\,\mathbf{a}_2 \times \mathbf{a}_3 \\
\mathbf{b}_2 &= \frac{2\pi}{V}\,\mathbf{a}_3 \times \mathbf{a}_1 \\
\mathbf{b}_3 &= \frac{2\pi}{V}\,\mathbf{a}_1 \times \mathbf{a}_2,
\end{aligned}$$

where V is the volume of the unit cell. The reciprocal lattice vector $\boldsymbol{G} = c_1\mathbf{b}_1 + c_2\mathbf{b}_2 + c_3\mathbf{b}_3$ can reach every point in the reciprocal space, which allows the analysis to be restricted to a unit cell in reciprocal space, called the first Brillouin zone [7].

2.2 Density functional theory

To study the electronic structure of materials, a widely used and effective method is density functional theory (DFT). DFT provides solutions to the otherwise unfeasible many-electron Schrödinger equation by using approximations which reduce the $3N$-dimensional problem to a 3-dimensional one. This framework enables the calculation of total energies and forces, paving the way to compute phonon dispersions, electronic band structures, and more. However, since DFT relies on approximations, it represents a trade-off between computational efficiency and accuracy.

In 1964, P. Hohenberg and W. Kohn published a paper that laid the theoretical foundation of density functional theory as we see it today. They showed that all properties of a quantum many-body system can be connected to functionals of the ground-state density [8]. However, their paper did not contain the way of constructing these functionals, and exact functionals for systems of many electrons are not known. Luckily, in 1965 W. Kohn and L. J. Sham formulated a way to approximate ground state functionals for many-electron systems which have paved the way for the wide application of DFT today.

2.2.1 Hohenberg-Kohn theorem

DFT is formally grounded in the Hohenberg-Kohn theorems, where the first theorem may be stated as follows:
The electron density determines the external potential, except for a constant.
This means that the electronic density defines the external potential, and as a consequence, the full Hamiltonian of the system. This implies that the many-electron wavefunction, and therefore all properties of the system, are given by only the ground state density. The Hamiltonian for a system of interacting electrons in an external potential is typically written as:

$$H = T + V_{\text{ext}} + V_{\text{ee}}. \tag{2.2}$$

Explicitly, it looks like:

$$\hat{H}(\mathbf{r}_1, \mathbf{r}_2, ..., \mathbf{r}_\text{N}) = -\sum_i \frac{1}{2}\nabla_i^2 + \sum_i V_\text{n}(\mathbf{r}_\text{i}) + \frac{1}{2}\sum_{\text{i}\neq\text{j}} \frac{1}{|\mathbf{r}_\text{i} - \mathbf{r}_\text{j}|}, \tag{2.3}$$

where the Hamiltonian includes the kinetic energy of the electrons, the Coulomb potential from the nuclei as seen by the electrons, and the interaction term between electrons. In any quantum state, the external potential uniquely determines the many-electron wavefunction, and the total energy is a functional of these wavefunctions.
The total energy in a many-electron system is given by:

$$E = \langle\Psi|\hat{H}|\Psi\rangle = \int \mathrm{d}\mathbf{r}_1 \ldots \mathrm{d}\mathbf{r}_n \, \Psi^*(\mathbf{r}_1, \ldots, \mathbf{r}_n) \, \hat{H} \, \Psi(\mathbf{r}_1, \ldots, \mathbf{r}_n). \tag{2.4}$$

Looking at equation (2.3), we see that the structure of the Hamiltonian is not dependent on the specific material, and thus the change in total energy must be associated with changes in the wavefunctions. This confirms the statement that the total energy is a functional of these wavefunctions, and combined with the first theorem, indicates that the total ground state energy is a functional of the ground state density.
The chronology can be written as follows:

$$n \to V_n \to \Psi \to E,$$

leading to the central result of DFT: $E = F[n]$ [9].
The second theorem confirms that the ground state energy is the lowest energy, using the variational principle which will be discussed further.
While the Hohenberg-Kohn theorem tells us that the total energy of the ground state is a functional of the electron density, it does not indicate the methodology for constructing such a functional. To date, the precise form of the functional is not known. Fortunately, several good approximations have been developed.

2.2.2 Kohn-Sham equations

To make DFT usable, Kohn and Sham introduced an approach where they made the ansatz of replacing the original many-body problem with a non-interacting (fictitious) reference system that yields the same ground-state density. This leads to the

Kohn-Sham equations, where $F[n]$ is decomposed into explicit and implicit terms. The implicit terms are then split into the kinetic and classical Coulomb energy of independent electrons and an exchange-correlation energy $E_{\mathrm{xc}}[n]$ that must be approximated.
The following functional can be written as:

$$\begin{aligned} E = F[n] = \int \mathrm{d}\mathbf{r}\, n(\mathbf{r}) V_n(\mathbf{r}) - \sum_i \int \mathrm{d}\mathbf{r}\, \phi_i^*(\mathbf{r}) \frac{\nabla^2}{2} \phi_i(\mathbf{r}) \\ + \frac{1}{2} \int \int \mathrm{d}\mathbf{r}\, \mathrm{d}\mathbf{r}' \, \frac{n(\mathbf{r}) n(\mathbf{r}')}{|\mathbf{r} - \mathbf{r}'|} + E_{\mathrm{xc}}[n], \end{aligned} \tag{2.5}$$

which includes the external potential, kinetic energy, classical Coulomb energy and exchange-correlation energy terms. This form breaks down the total energy in a sum of known and one unknown term.
The ground-state density n_0 is the one that minimizes the total energy $E = F[n]$ in accordance with the variational principle stated in the second Hohenberg-Kohn theorem. By minimizing the energy with respect to the fictitious Kohn-Sham orbitals (KS orbitals) $\phi_i(\mathbf{r})$, subject to the constraint that they remain orthonormal, one arrives at the Kohn-Sham equations:

$$\left[-\frac{1}{2} \nabla^2 + V_{\mathrm{n}}(\mathbf{r}) + V_{\mathrm{H}}(\mathbf{r}) + V_{\mathrm{xc}}(\mathbf{r}) \right] \phi_i(\mathbf{r}) = \varepsilon_i \phi_i(\mathbf{r}), \tag{2.6}$$

where $V_{\mathrm{H}}(\mathbf{r})$ is the classical Hartree potential, and the exchange-correlation potential is defined as the functional derivative:

$$V_{\mathrm{xc}}(\mathbf{r}) = \frac{\delta E_{\mathrm{xc}}[n]}{\delta n(\mathbf{r})}.$$

Since the exact form of $E_{\mathrm{xc}}[n]$ is unknown, various approximations are used in practice. The local density approximation (LDA) and generalized gradient approximation (GGA) are common, while there are more advanced functionals such as meta-GGA and hybrid functionals. They offer improved accuracy but at higher computational cost. The choice of functional is, as previously stated, a trade-off between computational cost and accuracy.

2.2.3 Exchange-correlation approximations

One of the simpler approaches to obtaining an expression for the functional is through the LDA, which estimates the exchange-correlation potential based on the local electron density. This approximation is effective because the exchange-correlation potential is typically much smaller than the kinetic potential and the Coulomb term in Eq. (2.5).
The LDA can be expressed as

$$E_{\mathrm{xc}}^{\mathrm{LDA}}[n(\mathbf{r})] = \int n(\mathbf{r}) \epsilon_{\mathrm{xc}}(n(\mathbf{r})) \mathrm{d}\mathbf{r},$$

where ϵ_{xc} is the exchange-correlation energy per particle of a uniform electron gas.

For greater accuracy, but at a slightly increased computational cost, we turn to density functionals that depend explicitly on both the electron density and its gradient. These are known as GGAs,

$$E_{\mathrm{xc}}^{\mathrm{GGA}}[n(\mathbf{r})] = \int n(\mathbf{r})\epsilon_{\mathrm{xc}}(n(\mathbf{r}), \nabla n(\mathbf{r}))\mathrm{d}\mathbf{r}.$$

A further refinement, meta-GGAs include not only the electron density and its gradient but also the kinetic energy density $\tau(\mathbf{r})$, which is expressed in terms of the KS orbitals [10]:

$$E_{\mathrm{xc}}^{\mathrm{MGGA}}[n(\mathbf{r})] = \int n(\mathbf{r})\epsilon_{\mathrm{xc}}(n(\mathbf{r}), \nabla n(\mathbf{r}), \tau(\mathbf{r}))\mathrm{d}\mathbf{r}.$$

2.2.4 Self-consistency

Having these functionals at hand, we can solve the Kohn-Sham equations by performing a self-constistent loop. The reason this is needed is because the total potential in equation (2.6) depends on the density, which in turn depends on the unknown eigenfunctions ϕ_i. What this means is that each solution depends on the other solutions. This is solved by guessing an electron density, insert it into the KS equations, obtain the wavefunctions ϕ_i and update the electron density via

$$n(\mathbf{r}) = \sum_i |\phi_i(\mathbf{r})|^2. \tag{2.7}$$

If the obtained electron density is the same as the initial one, within a specified tolerance range, the solution is found and the loop is terminated [9]. Once the electron density for the ground state is obtained, we can calculate the total energy using Eq. (2.5).

2.2.5 The Born-Oppenheimer approximation

The Born-Oppenheimer approximation is extensively used in DFT, in which we treat the heavy nuclei as fixed and consider only the electron positions. Thus we can decouple the positions of ions and electrons in the wavefunction. This allows the total wavefunction to be factorized into an electronic part and a nuclear part, effectively decoupling their motions:

$$\Psi(\mathbf{r}, \mathbf{R}) \approx \psi_e(\mathbf{r}; \mathbf{R})\chi(\mathbf{R}),$$

where $\mathbf{r}$ and $\mathbf{R}$ are electronic and nuclear coordinates, respectively. Here, $\psi_e(\mathbf{r}; \mathbf{R})$ is the electronic wavefunction for the given positions of the nuclei, and $\chi(\mathbf{R})$ is the nuclear wavefunction. This separation enables us to treat the electronic part independently, which is the focus of DFT.

2.3 Phonons

When discussing phonons, it is essential to move beyond the picture of fixed, motionless lattice ions. In reality, the ions in a crystal lattice oscillate around their

equilibrium positions. When energy is transferred to a single lattice ion, the energy will be distributed throughout the whole lattice as a result of the ion-ion interaction, leading to collective motion. These coupled oscillations are known as lattice vibrations and can be described quantum mechanically by transitioning to collective coordinates, where the resulting quanta are called phonons—quasiparticles that represent collective excitations.
Recalling the Born-Oppenheimer approximation, the kinetic energy of the lattice ions is given by

$$H_{i,kin} = \sum_{n\mu} \frac{p_{n\mu}^2}{2m_\mu}, \tag{2.8}$$

and the potential energy by

$$H_{ii} = V(\{\mathbf{R}_{n\mu}\}). \tag{2.9}$$

Here, $\{\mathbf{R}_{n\mu}\}$ is the momentary position of the μ-th atom in unit cell n and is decomposed as $\mathbf{R}_{n\mu} = \mathbf{R}_n^0 + \mathbf{R}_\mu + \mathbf{u}_{n\mu}$. $\mathbf{R}_n^0$, $\mathbf{R}_\mu$, $\mathbf{u}_{n\mu}$ are the position of the n-th unit cell relative to the origin, the position of the μ-th atom in the unit, cell and the displacement of atom μ in unit cell n from equilibrium, respectively. The quantity

$$V_0 = V(\{\mathbf{R}_n^0 + \mathbf{R}_\mu\}), \tag{2.10}$$

is the potential energy. By expanding V around the equilibrium position:

$$V(\{\mathbf{R}_{n\mu}\}) = V_0 + \sum_{n\mu\alpha} \varphi_{n\mu}^{\alpha} u_{\alpha n\mu} + \frac{1}{2} \sum_{n\mu\alpha} \sum_{n'\mu'\alpha'} \varphi_{n\mu n'\mu'}^{\alpha\alpha'} u_{n\mu\alpha} u_{n'\mu'\alpha'} + \mathcal{O}(u^3), \tag{2.11}$$

denoting α as Cartesian directions, and using the harmonic approximation, we can neglect the anharmonic terms. The force constant in the second term is zero due to the atoms being in equilibrium positions,

$$\varphi_{n\mu}^{\alpha} \equiv \left. \frac{\partial V}{\partial R_{n\mu\alpha}} \right|_0 = 0. \tag{2.12}$$

Considering the harmonic (second-order) approximation, the equations of motion for the ions can, through a sequence of transformations, be converted to equations of motion for a set of harmonic oscillators. This is a set of uncoupled equations, in contrast to the equations of motion for the ions. The Hamiltonian of the set of harmonic oscillators is

$$H_{\text{harmonic}} = \sum_{n\mu} \frac{(p_{n\mu}^{\alpha})^2}{2m_\mu} + \frac{1}{2} \sum_{n\mu\alpha} \sum_{n'\mu'\alpha'} \varphi_{n\mu n'\mu'}^{\alpha\alpha'} u_{n\mu\alpha} u_{n'\mu'\alpha'}. \tag{2.13}$$

The phonon modes and frequencies are given by the eigenvalue equation of this Hamiltonian, in the following form

$$\omega_{\mathbf{q}}^2 A_\mu^\alpha(\mathbf{q}) = \sum_{\mu'\alpha'} D_{\mu\mu'}^{\alpha\alpha'}(\mathbf{q}) A_{\mu'}^{\alpha'}(\mathbf{q}). \tag{2.14}$$

The dynamical matrix, defined as

$$D_{\mu\mu'}^{\alpha\alpha'}(\mathbf{q}) = \sum_n \frac{\varphi_{\mu\mu'}^{\alpha\alpha'}}{\sqrt{m_\mu m_{\mu'}}} e^{-i\mathbf{q}\cdot\mathbf{R}_n} \tag{2.15}$$

yields $3p$ eigenvalues for every crystal momentum vector $\mathbf{q}$, which can be either real or imaginary. The dispersion branches $\omega_j(\mathbf{q})$, where j is referred to as the band index, need to be determined for each direction $\mathbf{q}/|\mathbf{q}|$ due to crystals being anisotropic. For $q = 0$, the acoustic sum rule requires that there are three modes with zero frequency (acoustic modes), and the remaining $3p - 3$ modes are optical modes with non-zero frequencies.

Due to periodicity of the lattice, letting $\mathbf{G}$ be an arbitrary vector in the reciprocal space, we find that $\omega_j(\mathbf{q} + \mathbf{G}) = \omega_j(\mathbf{q})$. This means that we only need to consider the first Brillouin zone of the lattice. Also having time reversal symmetry leads to $\omega_j(\mathbf{q}) = \omega_j(-\mathbf{q})$.

For each of the ω_j values, the eigenvectors can be chosen so that an orthonormal relation is achieved

$$\sum_{\mu\alpha} A^{\alpha\,*}_{\mu j} A^{\alpha}_{\mu j'} = \delta_{jj'}. \tag{2.16}$$

This can be used to express the displacements $u^{\alpha}_{n\mu}$ in normal coordinates

$$u^{\alpha}_{n\mu}(t) = \frac{1}{\sqrt{N}} \frac{1}{\sqrt{m_\mu}} \sum_{j}^{3p} \sum_{\mathbf{q}} Q_j(\mathbf{q}, t) A^{\alpha}_{\mu j}(\mathbf{q}) e^{i\mathbf{q}\cdot\mathbf{R}^{\mathbf{0}}_{\mathbf{n}}}. \tag{2.17}$$

The lattice periodicity allows us to obtain an expression for the normal coordinates, by matrix inversion:

$$Q_j(\mathbf{q}, t) = \frac{1}{\sqrt{N}} \sum_{n\mu\alpha} \sqrt{m_\mu} u^{\alpha}_{n\mu}(t) A^{\alpha\,*}_{\mu j}(\mathbf{q}) e^{-i\mathbf{q}\cdot\mathbf{R}^{0}_{n}}, \tag{2.18}$$

which obeys the equation of motion of a harmonic oscillator. Now we can express our Hamiltonian in terms of normal coordinates,

$$H_{\text{harmonic}} = \frac{1}{2} \sum_{\mathbf{q}j} \left(\dot{Q}_j(\mathbf{q}, t)^* \dot{Q}_j(\mathbf{q}, t) + \omega_j^2(\mathbf{q}) Q_j(\mathbf{q}, t)^* Q_j(\mathbf{q}, t) \right). \tag{2.19}$$

To proceed in the form of second quantization, we start by transforming displacement and momentum into operators, whose commutation relations can be rewritten in terms of the normal coordinates Q. Using the momenta which are canonically conjugate to the normal coordinates, $\Pi_j(\mathbf{q}) = \dot{Q}_j(\mathbf{q})$, leads to the following commutation relations:

$$[\hat{Q}_j(\mathbf{q}), \hat{Q}_{j'}(\mathbf{q}')] = [\hat{\Pi}_j(\mathbf{q}), \hat{\Pi}_{j'}(\mathbf{q}')] = 0 \tag{2.20}$$

$$[\hat{\Pi}_j(\mathbf{q}), \hat{Q}_{j'}(\mathbf{q}')] = -i\hbar\, \delta_{jj'} \delta_{\mathbf{q}\mathbf{q}'}. \tag{2.21}$$

We introduce the annihilation and creation operators for phonons, in terms of normal coordinates and momenta as

$$b_{\mathbf{q}j} = \sqrt{\frac{1}{2\hbar\omega_j(\mathbf{q})}} \left(\omega_j(\mathbf{q}) Q_j(\mathbf{q}) + i\, \Pi_j(\mathbf{q}) \right) \tag{2.22}$$

$$b^{\dagger}_{\mathbf{q}j} = \sqrt{\frac{1}{2\hbar\omega_j(\mathbf{q})}} \left(\omega_j(\mathbf{q}) Q_j(\mathbf{q}) - i\, \Pi_j(\mathbf{q}) \right), \tag{2.23}$$

which follow the commutation relations of bosons:

$$[b_{\mathbf{q}j}, b_{\mathbf{q}'j'}] = [b^{\dagger}_{\mathbf{q}j}, b^{\dagger}_{\mathbf{q}'j'}] = 0 \tag{2.24}$$

$$[b_{\mathbf{q}j}, b^{\dagger}_{\mathbf{q}'j'}] = \delta_{\mathbf{q}\mathbf{q}'}\delta_{jj'}. \tag{2.25}$$

This yields the Hamiltonian for the quantized vibrations of the ion lattice:

$$H_{\text{harmonic}} = \sum_{\mathbf{q}j} \hbar\omega_j(\mathbf{q}) \left(b^{\dagger}_{\mathbf{q}j} b_{\mathbf{q}j} + \frac{1}{2} \right), \tag{2.26}$$

which forms the basis for electron-phonon coupling [11].

2.4 Electron-phonon coupling

After having quantized the ionic motion, we now want to investigate the interaction between the electronic and ionic subsystems.
The total Hamiltonian consists of three distinct subsystems

$$H = H_e + H_i + H_{e-i}, \tag{2.27}$$

where H_e is the electronic subsystem consisting of kinetic and Coulomb interactions,

$$H_e = \sum_{i}^{N_e} \frac{p_i^2}{2m} + \frac{1}{2}\frac{1}{4\pi\epsilon_0}\sum_{i\neq j}\frac{1}{|\mathbf{r}_i - \mathbf{r}_j|}, \tag{2.28}$$

while the ionic subsystem is defined in equations (2.8) and (2.9).
In this section, the coupled subsystems of electrons and ions are in the focus, described by the H_{e-i} term.

$$H_{e-i} = \sum_{i=1}^{N_e}\sum_{\alpha=1}^{N_i} V_{e-i}(\mathbf{r}_i - \mathbf{R}_\alpha) = H^{(0)}_{e-i} + H'_{e-i}. \tag{2.29}$$

The electron-phonon interaction implies the absorption and emission of phonons, and all interactions can be composed of four elementary processes, seen in Figure 2.1.
These interactions are reflected in the Hamiltonian, under the assumption that the ions are displaced as rigid bodies. Deformations represent higher-order effects, but in the harmonic framework we expand the interaction energy with respect to the atomic displacements only to the linear term.

$$V_{e-i}(\mathbf{r}_i - \mathbf{R}_\alpha) \equiv V_{e-i}(\mathbf{r}_i - (\mathbf{R}^0_\alpha + \mathbf{u}_\alpha)) = V_{e-i}(\mathbf{r}_i - \mathbf{R}^0_\alpha) - \mathbf{u}_\alpha \cdot \nabla V_{e-i} + \mathcal{O}(u^2_\alpha). \tag{2.30}$$

The second term in this expression contains the actual electron-phonon interactions, hence

$$H^{(1)}_{e-i} = -\sum_{i=1}^{N_e}\sum_{\alpha=1}^{N_i} \mathbf{u}_\alpha \cdot \nabla V_{e-i}. \tag{2.31}$$

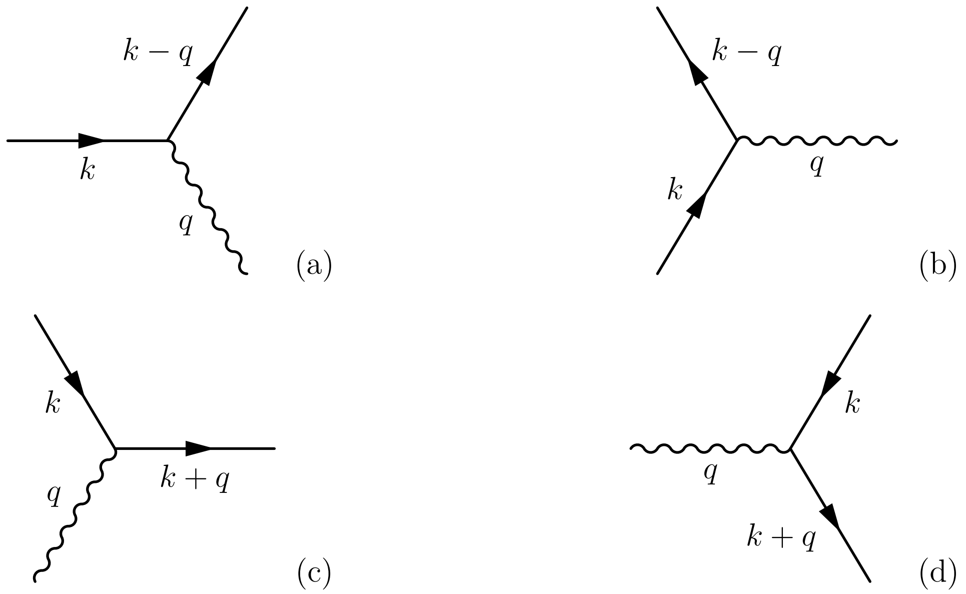

Figure 2.1: Feynman diagrams for four elementary electron-phonon interaction processes: (a) phonon emission by an electron; (b) phonon emission from electron-hole recombination; (c) phonon absorption by an electron; (d) creation of an electron-hole pair by phonon absorption.

Assuming singly-charged ions ($N_e = N_i = N$), reintroducing the indices from the previous chapter and using the expression for the atomic displacements in Eq. (2.17) yields

$$H^{(1)}_{e-i} = -\sum_{i}^{N} \sum_{n,\mu} \sum_{j}^{3p} \sum_{q}^{1.\mathrm{BZ}} \frac{1}{\sqrt{N m_\mu}} Q_j(\mathbf{q}) \mathbf{A}_{\mu j}(\mathbf{q}) e^{i\mathbf{q}\cdot\mathbf{R}^0_n} \cdot \nabla V_{e-i}(\mathbf{r}_i - \mathbf{R}^0_{n\mu}). \tag{2.32}$$

The first part of this equation is already familiar in second quantization. The electronic part can be expressed in second quantization the following way

$$\sum_{i}^{N} \nabla V_{e-i}(\mathbf{r}_i - \mathbf{R}^0_{n\mu}) = \sum_{kk'} \langle \mathbf{k} | \nabla V_{e-i} | \mathbf{k}' \rangle \, a^\dagger_{\mathbf{k}} a_{\mathbf{k}'}. \tag{2.33}$$

Using this result in equation (2.32), and the operator form of the normal coordinates, we can express the Hamiltonian for the electron-phonon interaction:

$$H_{e-p} = \sum_{\mathbf{k}} \sum_{\mathbf{q},\mathbf{G}} \sum_{\mu,j} T^{\mu j}_{\mathbf{k},\mathbf{q},\mathbf{G}} (b_{\mathbf{q}j} + b^\dagger_{-\mathbf{q}j}) \, a^\dagger_{\mathbf{k},\mathbf{q},\mathbf{G}} a_{\mathbf{k}}. \tag{2.34}$$

$T^{\mu j}_{\mathbf{k},\mathbf{q},\mathbf{G}}$ is the matrix element of the electron-phonon coupling, and is defined as

$$T^{\mu j}_{\mathbf{k},\mathbf{q},\mathbf{G}} = -i\sqrt{\frac{\hbar N}{2 m_\mu \omega_j(\mathbf{q})}} V^{\mu}_{e-i}(\mathbf{q}+\mathbf{G})[\mathbf{A}_{\mu j}(\mathbf{q})\cdot(\mathbf{q}+\mathbf{G})] \cdot \int \mathrm{d}^3\mathbf{r} u^*_{\mathbf{k}+\mathbf{q}+\mathbf{G}}(\mathbf{r}) u_{\mathbf{k}}(\mathbf{r}). \tag{2.35}$$

The interaction between electrons and phonons is responsible for several important physical phenomena, as illustrated by the four elementary processes in Figure 2.1.

Notably, it plays a central role in both electrical resistance and the formation of Cooper pairs—the foundation of superconductivity. In such a process, an electron emits a phonon, which is subsequently absorbed by another electron. This emission causes a distortion in the surrounding lattice by displacing the positively charged ions. The second electron responds to this deformation of the lattice, resulting in an effective electron-electron interaction. Unlike the usual Coulomb interaction, this interaction can be both repulsive and attractive. In the case of attraction, it can lead to the formation of electron pairs, known as Cooper pairs [11].

2.5 Born effective charges and polarization

The polarization $\mathbf{P}$ of a system determines several properties of the electrodynamics in solids, including certain light-matter interactions and ferroelectric phenomena [12, 13]. The Born effective charge (BEC) tensor $Z^*_{i\mu\nu}$ quantifies the relationship between the change in polarization and atomic displacements, and can be obtained by taking the derivative of the polarization with respect to atomic positions:

$$Z^*_{i\mu\nu} = \frac{\Omega}{e} \frac{\partial P_\mu}{\partial r_{i\nu}}. \tag{2.36}$$

Here, i is the atom index, e is the elementary charge, μ, ν denote Cartesian directions, and Ω is the unit cell volume. The polarization of the material can then be estimated using the computed Born effective charges and atomic displacements relative to a non-polar reference structure through the linearized expression:

$$P_\mu = \frac{e}{\Omega} \sum_{i\nu} Z^*_{i\mu\nu} \Delta u_{i\nu}, \tag{2.37}$$

where $\Delta u_{i\nu}$ is the atomic displacement of atom i along the Cartesian direction ν [12, 14]. Alternatively, the application of an electric field allows the Born effective charge tensors to be expressed as the derivative of the atomic forces $F_{i\nu}$ with respect to the electric field along μ E_μ,

$$Z^*_{i\mu\nu} = \frac{1}{e} \frac{\partial F_{i\nu}}{\partial E_\mu}. \tag{2.38}$$

This is obtained by combining the relations $P_\mu = -\partial U/\partial E_\mu$ and $F_{i\nu} = -\partial U/\partial r_{i\nu}$ [15].

A related quantity is the dielectric response function $\epsilon(\omega)$, which characterizes the response of the system to an oscillating electric field of frequency ω. It is a complex, frequency-dependent function:

$$\epsilon(\omega) = \epsilon_1(\omega) + i\epsilon_2(\omega), \tag{2.39}$$

where $\epsilon_1(\omega)$ and $\epsilon_2(\omega)$ are the real and imaginary parts, respectively.

When an oscillating electric field is applied, both the electrons and the ions respond, leading to an additional contribution to the dielectric permittivity at low frequencies. The ionic contribution is proportional to the BEC tensors, which determine the force

exerted on the ions by the field and the polarization created by their motion. This leads to the static dielectric constant $\epsilon(0)$, which can be significantly larger than the high-frequency electronic constant ϵ^{∞} where the electrons respond rapidly.
In the long wavelength limit, the real part of the dielectric response function is given by

$$\epsilon_1(\omega) = \epsilon^{\infty} + \frac{4\pi}{3\Omega}\sum_n \sum_{i\mu} \frac{|Z^*_{i\beta\mu} u^n_{i\mu}|^2}{\omega^2 - \omega_n^2}, \tag{2.40}$$

and the imaginary part by [16]

$$\epsilon_2(\omega) = \frac{4\pi^2}{3\Omega}\sum_n \sum_{i\mu} \frac{|Z^*_{i\beta\mu} u^n_{i\mu}|^2}{2\omega_n}\delta(\omega - \omega_n). \tag{2.41}$$

The Born effective charges directly describe the splitting between longitudinal and transverse optical modes (LO-TO splitting). In the long-wavelength limit of phonons, a macroscopic polarization and electric field is associated with the atomic displacements. The eigenfrequencies of phonons depend on the direction along which the limit is taken, and the polarization of the phonon [17].

2.6 Molecular dynamics

A well-established method for simulating the time evolution of a system of particles is through molecular dynamics (MD) simulations. From this, several properties can be calculated, such as the lattice thermal conductivity and the phonon density of states. To perform these simulations, the potential energy U is needed. For a system, the total potential energy can be described as

$$U = \sum_i U_i, \tag{2.42}$$

where the energy of each atom i is

$$U_i = U_i(\{\mathbf{r}_i\}). \tag{2.43}$$

The potential energy is used to construct an interatomic potential, typically generated using reference forces from DFT calculations. The interatomic potential is used to evaluate atomic forces. These forces describe how particles in the simulation will interact,

$$\mathbf{F}_i = -\frac{\partial U}{\partial \mathbf{r}_i}, \tag{2.44}$$

which is then used for integrating the equations of motion to evolve the system in time. This integration is typically done with the Verlet algorithm, where the time varying position of each particle is denoted by $\mathbf{r}_i(t)$. The velocities determine kinetic energy and temperature, and is denoted by $\mathbf{v}_i(t)$. The algorithm finds an expression that defines positions at time $t + \Delta t$ in terms of known positions at t, and is derived from the Taylor expansions of $\mathbf{r}_i(t)$. The formula reads as follows [18],

$$\mathbf{r}_i(t+\Delta t) \simeq 2\mathbf{r}_i(t) - \mathbf{r}_i(t-\Delta t) + \frac{\mathbf{F}_i(t)}{m_i}\Delta t^2. \tag{2.45}$$

When using GPUMD to perform MD simulations, the velocity Verlet algorithm, closely related to the algorithm above, is implemented. The key difference is that velocity and position are updated simultaneously according to [19]

$$\begin{aligned}\mathbf{v}_i(t+\frac{1}{2}\Delta t) &= \mathbf{v}_i(t) + \frac{1}{2}\frac{\mathbf{F}_i}{m_i}\Delta t,\\ \mathbf{r}_i(t+\Delta t) &= \mathbf{r}_i(t) + \mathbf{v}_i(t+\frac{1}{2}\Delta t)\Delta t,\\ \mathbf{v}_i(t+\Delta t) &= \mathbf{v}_i(t+\frac{1}{2}\Delta t) + \frac{1}{2}\frac{\mathbf{F}_i(t+\Delta t)}{m_i}\Delta t.\end{aligned} \tag{2.46}$$

2.6.1 Sampling the canonical ensemble

Due to the conservation laws following from the equations of motion, the microcanonical ensemble (NVE) is generated. In this ensemble, the number of particles N, volume V and energy E remain constant. Ensembles correspond to different experimental conditions; the NVE ensemble represents an isolated system of particles that does not interact with its surroundings.

However, to better mimic experimental conditions where the system can exchange heat with the environment, the canonical ensemble (NVT) is often used. In this ensemble, the temperature T is kept constant rather than the energy. To generate the canonical ensemble, introducing a thermostat is needed [20].

Several thermostats have been proposed for MD simulations; one example is the Berendsen thermostat.

The Berendsen thermostat uses velocity rescaling to control the temperature, adjusting particle velocities toward a target temperature. This leads to a proportional scaling of the velocities per time step as

$$\mathbf{v}_i \to \lambda \mathbf{v}_i, \ \lambda = \sqrt{1 + \frac{\Delta t}{\tau_T}\left(\frac{T_0}{T} - 1\right)} \tag{2.47}$$

where τ_T is the coupling time constant, T_0 is the target temperature, and T is the current temperature [21].

Due to the high computational cost of DFT, these approaches are limited with respect to system size and complexity [22]. For this purpose, neuroevolution potential (NEP) models have been developed, providing a compromise between accuracy and computational efficiency.

2.7 Neuroevolution potential models

Neural network-based machine learning potentials are trained on DFT data to perform large-scale MD simulations. In this work, neuroevolution potential (NEP) models are used as an effective potential in MD simulations. The forces are obtained by relating the output energy from Eq. (2.48) to atomic forces, as shown in equation Eq. (2.44). The neural network model is a simple feed-forward network with one hidden layer,

$$U_i = \sum_{\nu=1}^{N_{\text{neu}}} w_{\mu}^{(2)} \tanh \left(\sum_{\nu=1}^{N_{\text{des}}} w_{\mu\nu}^{(1)} q_{\nu}^{i} - b_{\mu}^{(1)} \right) - b^{(2)}. \tag{2.48}$$

N_{neu} is the number of neurons in the hidden layer, N_{des} is the number of descriptor components, w are the weights and b are the biases.

$\tanh(x)$ is the activation function in the hidden layer, and the total number of parameters in the neural network equals $(N_{\text{des}} + 2)N_{\text{neu}} + 1$. The descriptor vector contains radial descriptor components and three, four, and five-body descriptor components. Recently, the NEP framework was generalized to enable prediction of rank one and two tensors via the tensorial neuroevolution potential (TNEP) scheme. This enables construction of models for polarizability and dipole moment.

The methodology is similar to performing MD with regular NEP models, but instead of using energy and forces for training, the TNEP framework uses physical quantities such as polarizability and susceptibility. The workflow still uses regular NEP models for constructing PES and generate the MD trajectory, while the TNEP approach predicts the specified quantities for the specific frames in the trajectory [23].

In this work, the TNEP framework will be used to predict the Born effective charges during MD simulations for several space groups of $CaTiO_3$.

3

Perovskites

3.1 Halide perovskites

Halide perovskites (HPs) are a class of materials that meet many of the current requirements for efficient photovoltaic conversion, and have been among the most intensively studied materials in recent years [24]. HPs are emerging as promising materials across a range of applications, such as solar cells, light-emitting diodes (LEDs), and photodetectors. However, their practical deployment is hindered by their sensitivity to environmental factors, such as temperature and humidity, which leads to rapid degradation. Furthermore, the presence of toxic elements like lead raises environmental and health concerns, creating a demand for safer alternatives. Perovskites are crystalline solids with the general chemical formula ABX_3, where, in the case of simple HPs, A represents a monovalent cation, B a divalent cation, and X the halogen [25].

A monovalent cation carries a +1 charge, meaning it has lost one electron. A divalent cation carries a +2 charge, having lost two electrons. The halogen ions form octahedral shapes with a divalent cation in the centre, and a monovalent cation is located between the octahedra. Sometimes, the A site is occupied by an organic cation, such as methylammonium. However, inorganic species such as Cs and Rb are common as well. The structure of a simple HP is visualized in Figure 3.1.

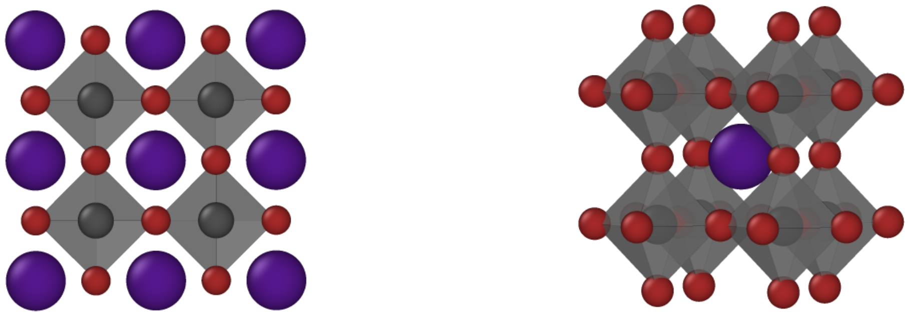

Figure 3.1: Crystal structure of halide perovskite $CsPbBr_3$, where Cs ions are shown in purple and Br ions in red. The Pb ions are located at the centres of the grey $PbBr_6$ octahedra.

Perovskites often exhibit phonon instabilities in their cubic phase, which can manifest as cation displacements and tilting of the octahedra. Of particular interest is the octahedral tilting, as it is closely linked to changes in the electronic structure. Exposure to varying temperatures can induce phase transitions that involve distortions in the crystal lattice and are often associated with octahedral tilting. At high temperatures, the cations occupy positions consistent with a cubic structure, characterized by high-symmetry. As the temperature decreases, the system transitions to lower-symmetry phases such as the tetragonal or orthorhombic structures. The octahedral tilting is associated with specific phonon modes: the in-phase tilting mode (M-point), and the out-of-phase tilting mode (R-point), which appear as negative frequencies in the phonon dispersion shown in Figure 4.1 [26, 27].

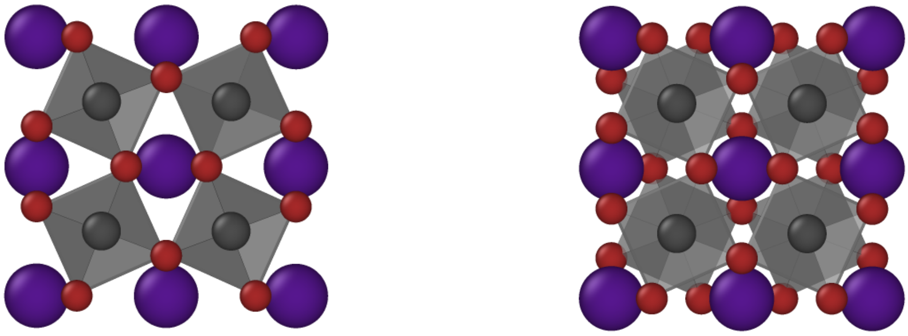

Figure 3.2: In-phase tilting M point mode (left), out-of-phase tilting R point mode (right).

The structural stability of perovskites can be qualitatively measured by the Goldschmidt tolerance factor, t, which is calculated from the ionic radius of the atoms:

$$t = \frac{r_\mathrm{A} + r_\mathrm{X}}{\sqrt{2}(r_\mathrm{B} + r_\mathrm{X})}. \tag{3.1}$$

Where r_A is the radius of the A cation, r_B is the radius of the B cation, and r_X the radius of the anion. Generally, materials with a tolerance factor between 0.9 and 1.0 are expected to have an ideal cubic structure. For tolerance factors between 0.71 and 0.9, the perovskite structure often becomes distorted due to tilting of the octahedra. Outside these ranges, non-perovskite structures are formed [28].

3.2 Ruddlesden-Popper phases

Recently, so-called two-dimensional perovskites have gained significant attention, consisting of stacked inorganic perovskite layers separated by either organic or inorganic cations. One important class of these two-dimensional perovskites is the Ruddlesden-Popper (RP) phases. They are of interest because they exhibit improved stability compared to the regular three-dimensional perovskites. However, RP phases that include interleaved organic layers tend to show larger exciton binding energy due to the dielectric mismatch between the organic and inorganic layers [29].

This leads to worse photovoltaic performance compared to three-dimensional perovskites, but they are better suited for other optoelectronic devices such as LEDs and photodetectors. The general formula of Ruddlesden-Popper phases is $A_{n+1}B_nX_{3n+1}$, where n is the number of perovskite layers. As in three-dimensional perovskites, A and B are cations and X is an anion.
Perovskite oxides, specifically the RP type perovskite oxides ($A_{n+1}B_nO_{3n+1}$), exhibit interesting properties for ferroelectrics. One such property is known as hybrid improper ferroelectricity, and largely originates from the rotation of the octahedra [30, 31]. The n perovskite layers (ABO_3) alternate with rock-salt layers (AO) along the crystallographic c-direction. The crystal structures of the oxide RP phases for $n = 1$ to $n = 3$ with space group $I4/mmm$ are illustrated in Figure 3.3, which visualizes how the structure evolves with increasing layer number.

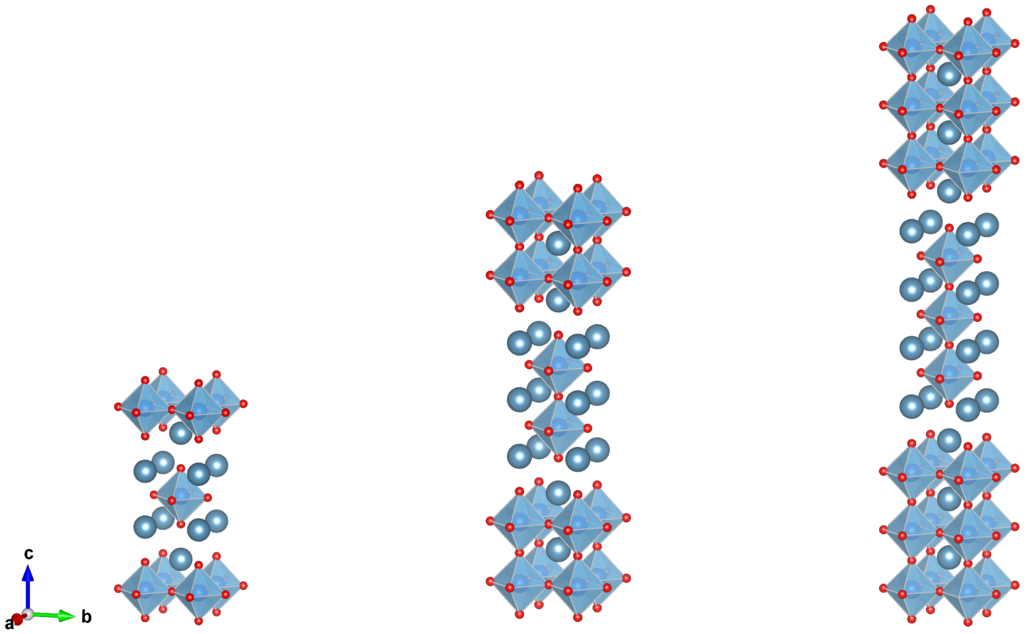

Figure 3.3: Crystal structures of different $I4/mmm$ oxide RP phases. From left to right: $n = 1$ Ca_2TiO_4, $n = 2$ $Ca_3Ti_2O_7$, and $n = 3$ $Ca_4Ti_3O_{10}$.

The RP phase $Ca_3Ti_2O_7$ has been confirmed to undergo a phase transition from a high-temperature non-polar phase to a low-temperature polar phase. The remanent ferroelectric polarization–the portion that remains after an external field is removed–has been determined to be approximately $8\,\mu C/cm^2$ [32].
RP phases offer extensive opportunities for tuning material properties by varying parameters such as the number of perovskite layers and chemical composition. A wide range of RP variants are actively being investigated to explore a broad range of phenomena such as excitonic behavior and oxygen mobility [33, 34]. These investigations are essential for developing new energy materials and meeting future needs for energy conversion.

4

Results

The following chapter presents the methodology and results obtained throughout the project. It begins with the investigation of electron-phonon coupling in the halide perovskite $\mathrm{CsPbBr_3}$, where phonon mode coordinates were analyzed to assess their influence on the band gap and to develop a model that describes the behavior of the valence band maximum (VBM) at 400 K. Subsequently, the chapter proceeds with the findings from the study of the $\mathrm{CaTiO_3}$ perovskite and several RP phases, where a tensorial neuroevolution potential (TNEP) model was constructed to predict BECs. The resulting charges were then used to predict the polarization of the material, and comparisons were made against DFT and experimental data.

To assess the problem statement, large-scale MD simulations using GPUs were performed using the `GPUMD` package, and the outputs were analyzed with use of the `Python` package `calorine` [35, 36]. All calculations and the following analysis were conducted using `Python`, and the atomic structures were handled using the atomic simulation environment (`ASE`) package [37]. During all MD simulations, the potential energy was modeled using neuroevolution potential (NEP) models that have been trained on DFT data for the respective systems [38].

Throughout the project, DFT calculations were conducted using the Vienna Ab initio Simulation Package (VASP).

4.1 Halide perovskite $CsPbBr_3$

To obtain an overview of the material properties, the phonon dispersion relation was calculated. The dispersion relation describes how phonons propagate through the crystal lattice and connects the wave vector with their frequency, which is crucial for determining thermal properties. The phonon dispersion of $CsPbBr_3$ for the relaxed primitive cubic structure is visualized in Figure 4.1.

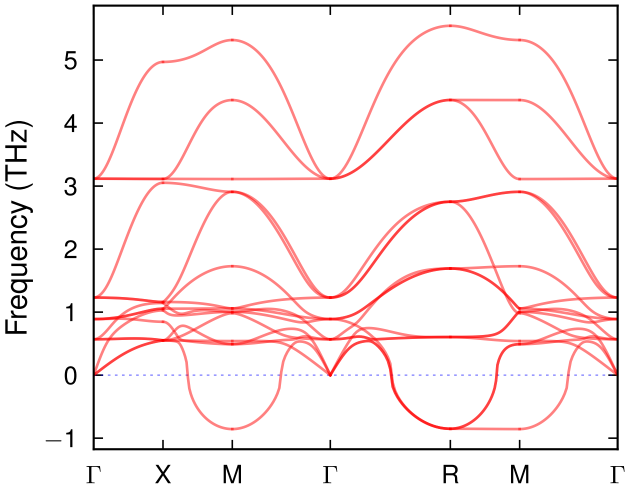

Figure 4.1: Phonon dispersion for the cubic structure. The labels correspond to points in the Brillouin zone, $\Gamma\,[0,0,0]$, $X\,[0.5,0,0]$, $M\,[0.5,0.5,0]$ and $R\,[0.5,0.5,0.5]$. Imaginary frequencies are denoted by negative numbers on the y-axis.

We observe that imaginary modes, indicated by negative frequencies, are found at the R- and M-symmetry points, having the $\mathbf{q}$-values $[0.5,0.5,0.5]$ and $[0.5,0.5,0]$ respectively. These modes induce the octahedral tilting of the perovskite structure seen in Figure 3.2, and indicate the presence of structural instabilities, as the cubic phase is not the true ground-state structure. The phonon dispersion was produced using the `Phonopy` package [39].

4.1.1 Phase transitions and lattice parameter extraction

Heating and cooling simulations were performed using `GPUMD` in the isothermal–isobaric (NpT) ensemble, with a time step of 1 fs, starting the heating simulation from the orthorhombic structure and the cooling simulation from the cubic structure. This was done for a large system of 20480 atoms, obtained by a 16 × 16 × 16 repetition of the primitive cell. From Figure 4.2, it is evident that the cubic phase has been reached at 400 K, as indicated by the convergence of the lattice parameters. Further investigation of $CsPbBr_3$ was performed at this temperature in the cubic phase.

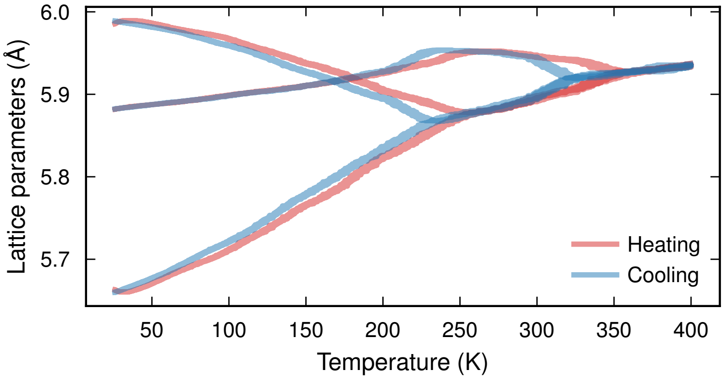

Figure 4.2: Heating (red) and cooling (blue) simulations of $CsPbBr_3$ to determine the temperature at which the cubic phase becomes stable.

At 400 K, another MD simulation was carried out in the NpT ensemble to extract the lattice parameter for the supercell at this temperature, which is seen in Figure 4.3.

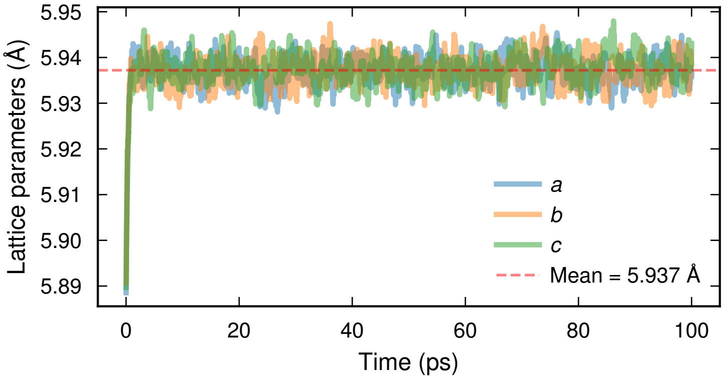

Figure 4.3: Convergence of the lattice parameters during an MD simulation in the NpT ensemble at 400 K over 100 ps.

The lattice parameters quickly converges to an average value of 5.397 Å, indicating a cubic structure. This value was then extracted and used for further analysis of the phonon modes at constant temperature for a smaller supercell.

4.1.2 Band gap evolution from phonon mode distortion

By distorting the crystal structure along a phonon eigenmode, the change in potential energy as a function of the displacement factor λ can be calculated. For harmonic phonon modes the energy follows a parabola with a minimum at $\lambda = 0$ (no distortion), while for imaginary phonon modes (M, R) a double-well potential energy surface is observed. As discussed in Section 3 and illustrated in Figure 3.2, these double wells represent structural instabilities associated with octahedral tilting, indicating that the undistorted phase is not a true local minimum on the potential energy surface. The structure can lower its energy by distorting along the imaginary modes, leading to lower-symmetry structures. This analysis was performed using a 40 atom cubic structure (repeated 2 × 2 × 2) at 400 K for the imaginary phonon modes as well as a real phonon mode at the X-symmetry point, with phonon eigenvectors obtained using `Phonopy`. The expected anharmonicity was observed during

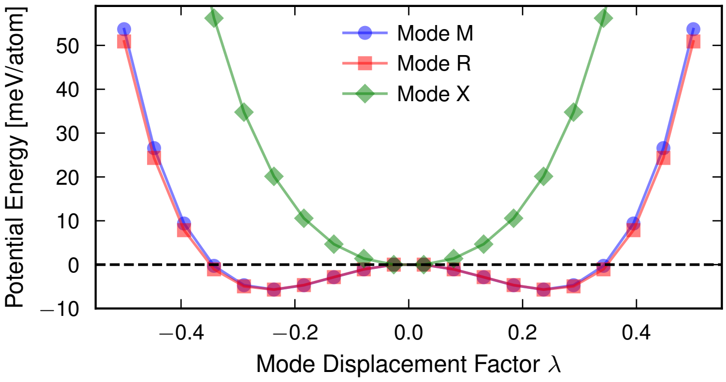

Figure 4.4: Potential energy surface associated with the tilt modes at the M-, R- and real X-point. Zero energy refers to the structure with no distortion. The displacement factor λ refers to the scalar factor applied to each phonon eigenvector, where we observe the energy minima of the imaginary modes at $\lambda = \pm 0.237$. For the modes shown here, the eigenvectors have the same magnitude, allowing for direct comparison using λ.

displacement along the tilt modes, and harmonicity along the real mode. For the X-point mode, the energy minimum occurs at $\lambda = 0$, indicating that the structure is stable with no distortion along this mode. In contrast, at the R- and M-point modes, the undistorted structure is unstable, and the system lowers its energy by displacing along these modes, leading to lower symmetry phases. For the tilt modes, the well depth indicates the energy difference between the distorted structure and the non-distorted cubic phase, and is 5.37 meV per atom for a displacement factor of $\lambda = \pm 0.237$.

The influence of the M-, R-, and X-point phonon modes on the electronic structure was further examined by evaluating the evolution of the band gap as a function of the displacement factor λ. To do this, a series of structures was generated corresponding to incremental values of λ, and their band gaps were computed using VASP with the meta-GGA exchange-correlation functional SCAN (Strongly Constrained and Appropriately Normed).

As shown in Figure 4.5, for both imaginary and real phonon modes, the band gap increases as the structure is displaced along the respective phonon eigenvectors, although the degree of increase varies. This suggests that deviations from the high-symmetry cubic phase lead to an increase of the band gap for this perovskite. The band gap for the undistorted structure is calculated to be $E_{\mathrm{bg}} = 1.82\,\mathrm{eV}$. As shown in Figure 4.4, the energy increases quadratically for large displacement factors beyond the well minima. In this regime, the atomic configurations become increasingly distorted, and the calculated band gap values exhibit non-physical trends. As a

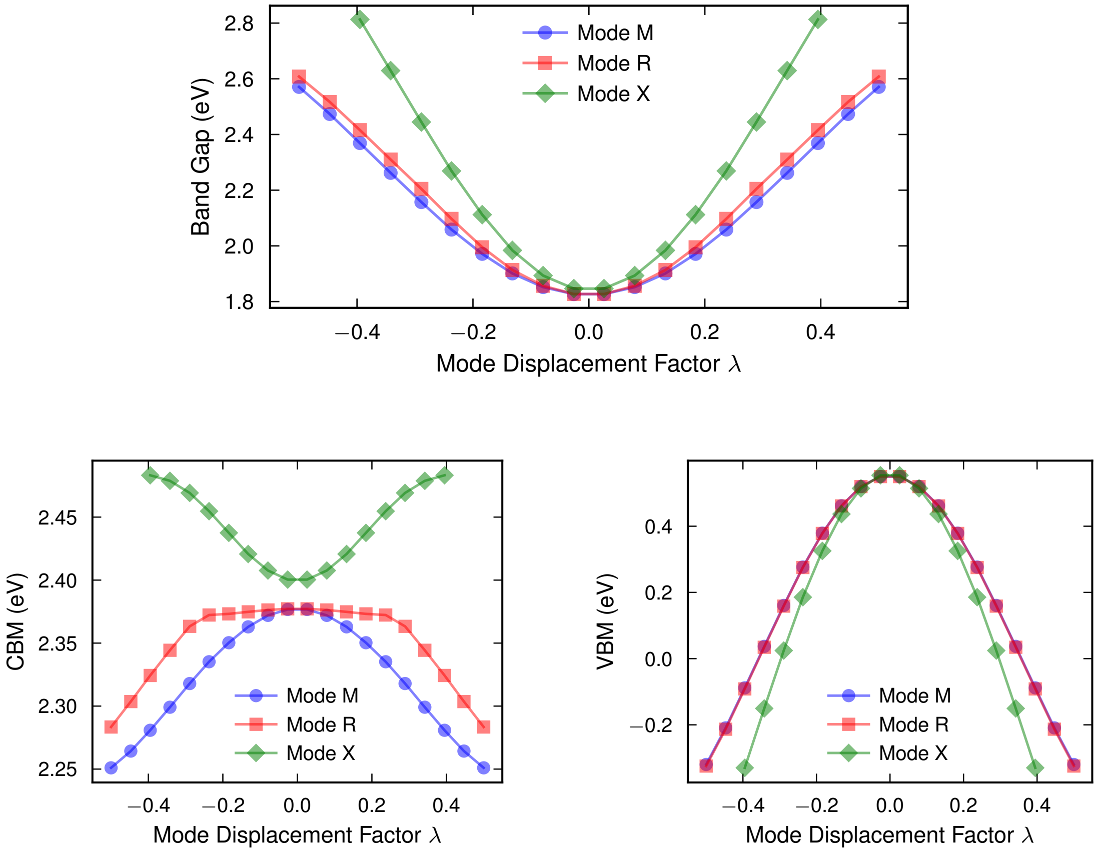

Figure 4.5: Band gaps and the corresponding CBM and VBM values associated with the M-, R- and X-point modes. At $\lambda = 0$ the band gap is 1.82 eV. It is observed that the imaginary modes widen the band gap.

result, only displacements within the region of the double-well minima correspond to realistic lattice dynamics. Beyond this region, the potential energy surface steepens rapidly, indicating that such configurations are no longer representative of physically meaningful structures.

The observed increase in band gap when displacing the structure along these phonon modes indicates a significant degree of electron-phonon coupling at this temperature. This demonstrates that specific vibrational modes, especially those associated with structural instabilities, can strongly influence the electronic structure.

To further investigate the behavior of the band gap in the undistorted cubic phase, 500 snapshots were extracted from a 20 ps MD simulation in the NVT ensemble. For each snapshot, the corresponding band gap was calculated to track its time evolution.

Figure 4.6 reveals that the band gap fluctuates significantly over time, due to thermal lattice vibrations. It is of particular interest to identify which phonon modes contribute most to these fluctuations.

The mode coordinates $Q_n(t)$ can be determined through phonon mode projection, in which the atomic displacements $\mathbf{u}(t)$ are projected onto the phonon mode eigenvector

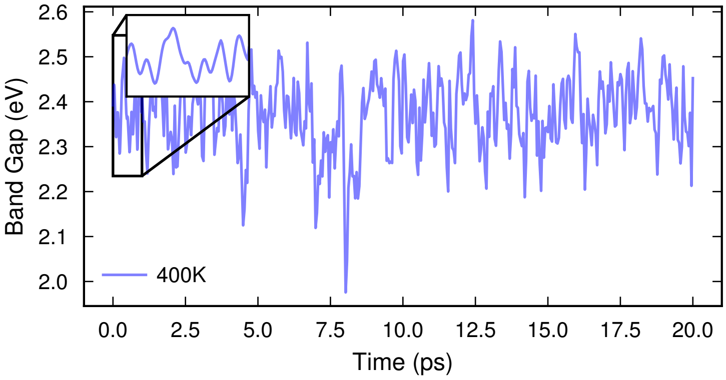

Figure 4.6: Band gaps obtained from DFT during a 20 ps MD simulation at 400 K. Band gaps were extracted every 1 fs during the first picosecond, and every 0.047 ps for the remaining 19 ps.

$\mathbf{e}_n$ according to $Q_n(t) = \mathbf{u}(t) \cdot \mathbf{e}_n$. This is visualized for the X-point mode in Figure 4.7. The displacements were obtained using the `hiphive` package, which provides the smallest displacement between the ideal structure and the displaced structure during an MD simulation [40].

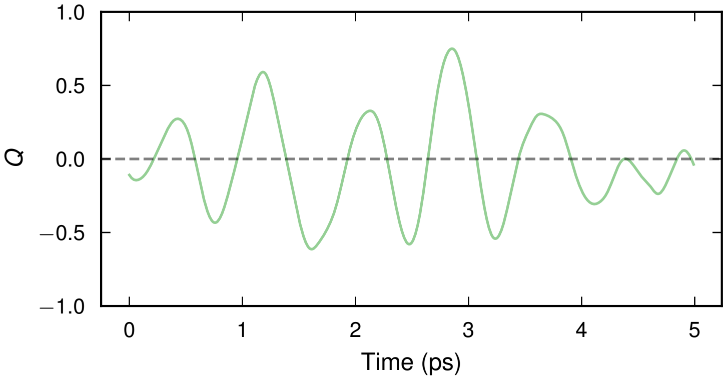

Figure 4.7: Time evolution of the mode coordinate $Q(t)$ for the harmonic X-point mode, projected from MD displacements at 400 K.

During these simulations, a single simulation cell was used, using periodic boundary conditions to mimic a simulation in a larger space. If an atom moves out of the simulation cell, the atom is wrapped back into the cell. `hiphive` accounts for this by assuming periodic boundary conditions in all directions, ensuring that the correct displacement is calculated when atoms cross the periodic boundaries.

4.1.3 Feature-based modeling of VBM fluctuations

The band gap is defined as the energy difference between the conduction band minimum (CBM) and the valence band maximum (VBM). While both band edges contribute to the band gap, this analysis focuses specifically on modeling the behavior of the VBM.

In the simulation presented in Figure 4.6, the squared mode coordinates Q^2 for all phonon modes were extracted alongside the corresponding VBM values for each snapshot in time. Here, the VBM refers to the highest valence band energy across all bands and **k**-points at a given snapshot. The use of squared coordinates was motivated by the approximately parabolic relationship observed between mode displacement and band gap, as seen in Figure 4.5. While the relationship is not perfectly quadratic, it provides a starting point for modeling. However, several forms of mode coordinate dependence were explored independently, including linear, quadratic, higher-order, and interaction terms. A simplified general expression for the band edge energy is:

$$\varepsilon(Q) = \varepsilon_0 + \sum_n a_n\, Q_n + \sum_n b_n\, Q_n^2 + \sum_{n \neq m} d_{mn}\, Q_m Q_n + \sum_n c_n\, Q_n^4 + \mathcal{O}(Q^6), \qquad (4.1)$$

where a, b, d and c are fitted coefficients. Here ϵ_0 is a constant representing the baseline energy level. In the modeling context, it functions as a bias term and was implemented as a column of ones, enabling the model to learn the overall baseline around VBM fluctuations. Among these individual terms, the quadratic dependence of Q_n, combined with the bias term, provided the best agreement with DFT data.

Using the squared phonon mode coordinates as input, a model was developed to describe the time-dependent fluctuations of the VBM. Although the band gap depends on both the VBM and the CBM, the underlying relationship between mode coordinates and either band edge is similar. Thus, the analysis focuses solely on the VBM to reduce complexity while still capturing the coupling between lattice dynamics and electronic structure. The model takes the following form:

$$\varepsilon_{\mathrm{VBM}}(t) = \epsilon_0 + \sum_n b_n Q_n^2(t). \qquad (4.2)$$

The goal was to determine how many of the 120 phonon modes contribute significantly to the variation in the VBM, and to identify which specific modes have the most impact. In the context of the modeling analysis, these mode contributions will be referred to as features.

Two different feature selection methods were evaluated: Recursive feature elimination (RFE) and automatic relevance determination regression (ARDR). RFE is a feature selection method that helps identify the most important features of a dataset, and works by starting with all features in the training dataset and iteratively fitting the data, ranking features by importance, and discarding the least important features. ARDR is a Bayesian regression approach that assigns different relevance weights to each feature, automatically determining their importance during the fitting process. Both methods were accessed using the `trainstation` package, which provides a convenient interface to `Scikit-Learn`. [41, 42].

These methods were evaluated using a random 90:10 train/test split of the data to evaluate performance, and the resulting root mean squared error (RMSE) over number of non-discarded features was compared for case.

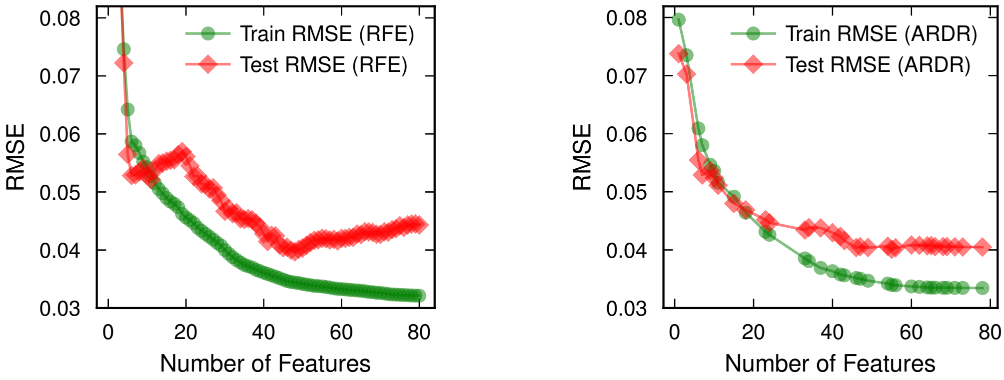

(a) RFE

(b) ARDR

Figure 4.8: RMSE of each feature selection method as a function of the number of features.

As seen in Figure 4.8, the overall performance between RFE and ARDR is comparable in terms of RMSE. The RMSE curves show that the models with fewer features align train and test RMSE better, but this comes at the cost of higher overall error, indicating underfitting. ARDR appears particularly promising with 20 features, suggesting a potentially optimal feature subset.
It is worth noting that this is a particularly challenging dataset due to the rapid fluctuations of both the VBM values and the projected mode coordinates, adding complexity to the modeling process. This may explain anomalies such as the RMSE spike in RFE around 20 features.

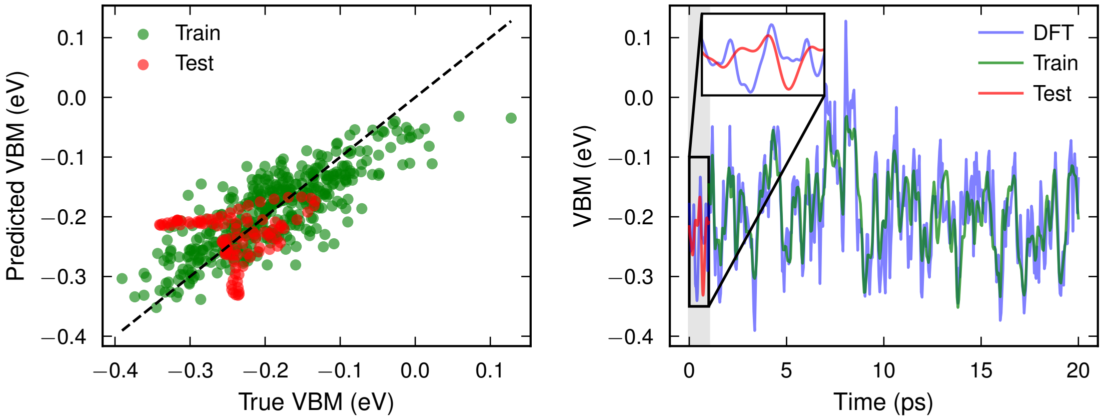

(a)

(b)

Figure 4.9: Model performance using ARDR with 20 features against DFT data: (a) parity plot comparing predicted and true VBM values; (b) VBM prediction using the first picosecond as test.

However, as seen in Figure 4.9, the ARDR model using 20 features struggles to predict the VBM fluctuations accurately, despite the favorable RMSE. In this case, the model was trained on the final 19 ps of the trajectory and tested on the first picosecond. The inconsistency may arise because the RMSE, computed over the test set, can appear low if the model captures overall trends, even while failing to reproduce short-timescale fluctuations in the VBM.
Given the performance of ARDR, further analysis focused on the RFE approach. Using the same train/test split, RFE was applied to evaluate how well different numbers of features capture the VBM fluctuations. Specifically, models using 10 and 40 out of 120 features were compared, where 40 features were chosen based on the best observed performance, and 10 were included as a reference point.

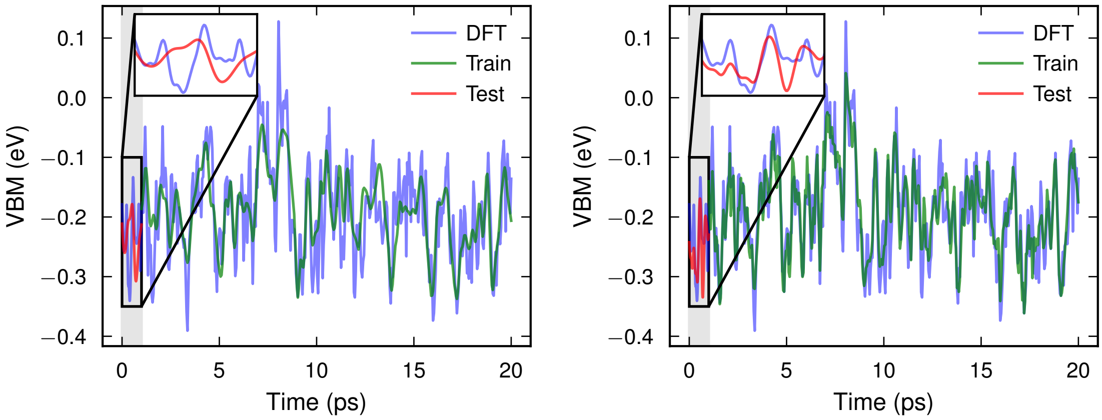

(a) **(b)**

Figure 4.10: Comparison of model performance against DFT data using (a) 10 features and (b) 40 features.

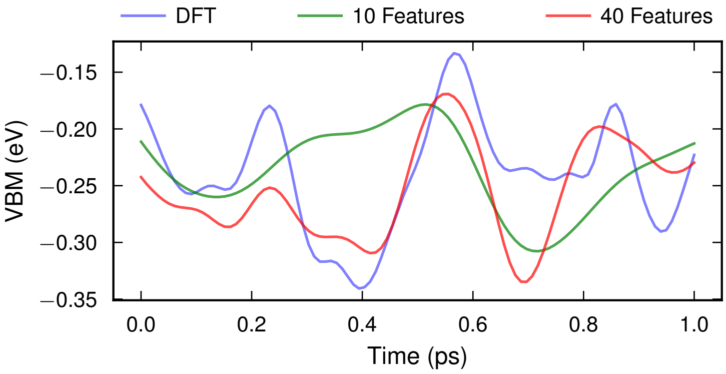

Figure 4.11: Test set comparison of VBM model predictions using 10 features (green) and 40 features (red) compared to DFT data (blue).

As shown in Figure 4.10 and 4.11, the 10-feature model fails to capture the rapid fluctuations in the VBM, while the 40-feature model performs significantly better.

This improvement suggests that several modes contribute non-negligibly, rather than a few dominant ones. Thus, the 10-feature model underfits the system, and fails to account for all types of structural distortions that influence the VBM. Increasing the number of features beyond 40 leads to more complex models but does not yield improved predictive performance. A model with all available features tends to overfit and generalize poorly, indicating that additional features provide limited benefit to model performance. The 40-feature model thus offers a balanced trade-off between capturing fluctuations and maintaining control over overfitting.
To better illustrate these trends, parity plots were generated for models using 10, 40, and 90 features:

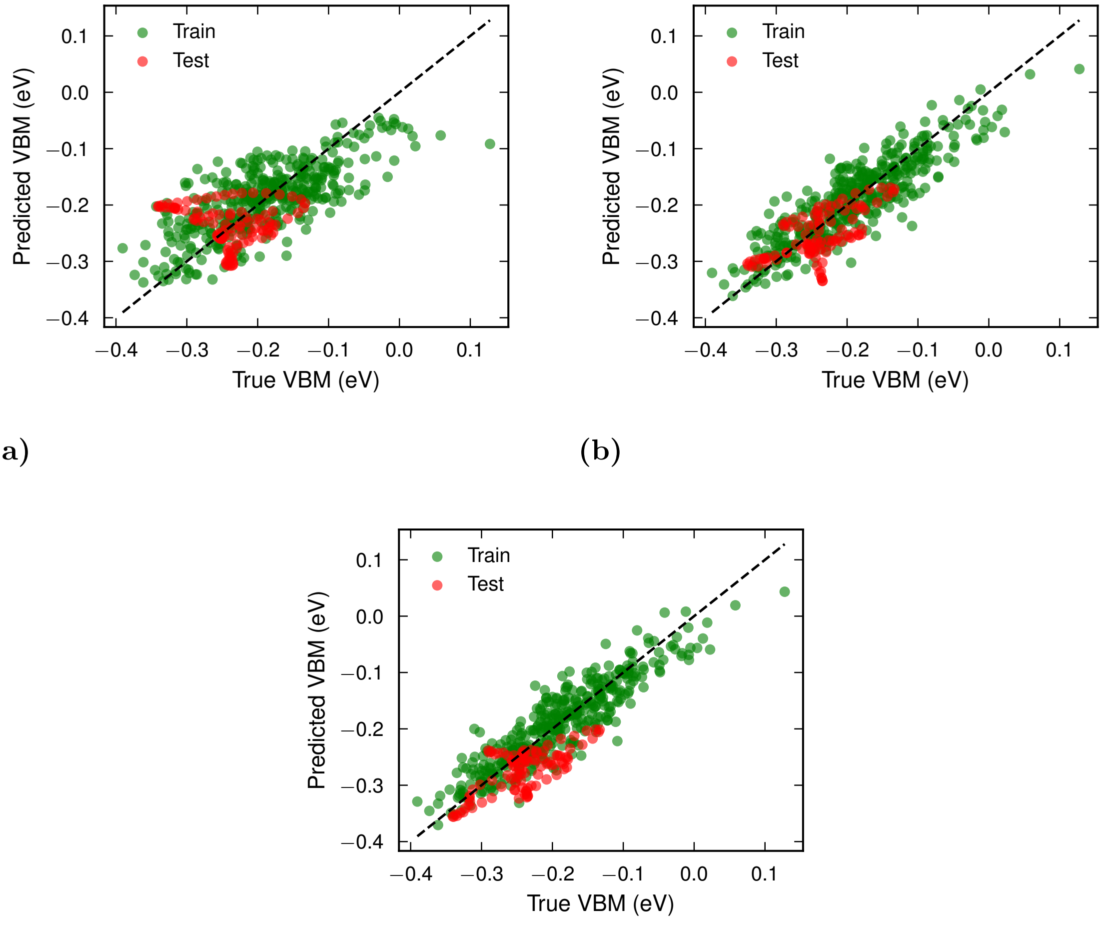

(a)

(b)

(c)

Figure 4.12: Parity plots showing predicted versus actual VBM values for (a) the 10-feature model, (b) the 40-feature model, and (c) the 90-feature model. Accuracy improves significantly between (a) and (b), but improvement halts beyond 40 features.

These plots again show a significant increase in accuracy for the 40-feature model. As seen in Figure 4.12c, the performance of a model using 90 features remains comparable to that of the 40-feature model, confirming that increasing the number of features beyond 40 does not lead to a significant improved accuracy.

As previously stated, it is of interest to evaluate which modes contribute most to the fluctuations in the VBM. From Eq. (2.35), it is clear that low-frequency modes are expected to couple more strongly, due to the ω^{-1} dependence of the matrix element. The `trainstation` package provides a function that returns the average contribution of each feature in the input data after applying RFE. Using this function, the top 10 most contributing modes were extracted, and are displayed in the phonon dispersion shown in Figure 4.13.

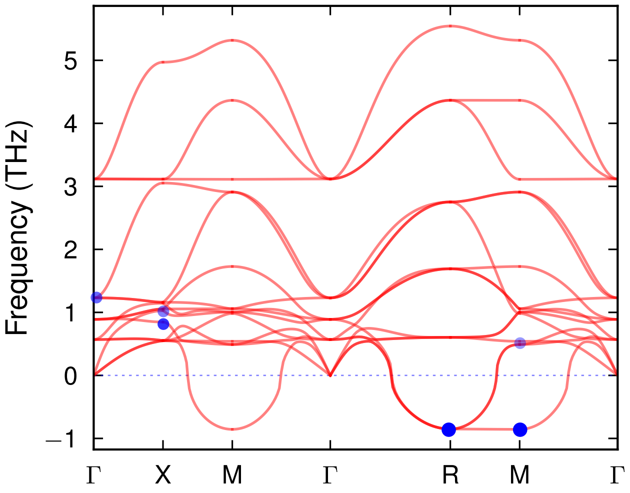

Figure 4.13: Phonon dispersion of $CsPbBr_3$ with the most influential modes marked. Only six modes are marked, due to several top-ranked modes having equivalent contributions across different polarization directions at the same **q**-point. The opacity indicates each mode's rank in the top 10, while the size reflects the presence of multiple polarization components.

As expected we find that all Cartesian components of the imaginary R- and M-point modes rank among the top 10 features. This is expected, as tilt modes are associated with phase transitions and are known to strongly influence the electronic properties of materials. A more complete model is likely to require combinations of mode coordinates, including cross-terms. Nonetheless, it is notable that this simple model–using squared mode coordinates only–captures VBM fluctuations reasonably well without explicitly modeling the full nonlinearity of the system.

Overall, this provides a proof of concept that VBM fluctuations can be reasonably well modeled using only a fraction of the available phonon modes and a simple relation to the VBM. By identifying the most relevant modes, the model provides insight into which vibrational modes couple most strongly to the electronic properties, offering an overview of the electron-phonon coupling in the material. While a larger dataset could potentially improve the model's accuracy, the rapid fluctuations in both the VBM values and mode coordinates are likely to remain a limiting factor. Future work could extend this analysis to model specific **k**-points in the band structure and explore the influence of phonon modes on flat bands, providing further understanding of local changes in electronic structure.

4.2 Born effective charges for $CaTiO_3$

Calcium titanate ($CaTiO_3$) is an inorganic oxide with a perovskite structure and is nominally non-polar. The RP ($n = 2$) phase $Ca_3Ti_2O_7$, however, exhibits ferroelectric properties. Whether a material can exhibit properties such as ferroelectricity depends on its crystal symmetry, as described by Neumann's principle.

In this work, the BECs of $CaTiO_3$ were investigated across several crystal structures, including the perovskite structure and RP phases with $n = 1$ to $n = 4$ and $n = 8$. The studied space groups include $Pnma$ (perovskite), $Pbca$ ($n = 1$), $Cmc2_1$ ($n = 2$), $Pbca$ ($n = 3$), and $Cmc2_1$ ($n = 4$ and $n = 8$).

The BECs are directly linked to the electron-phonon coupling, as they quantify the coupling between electric fields and lattice vibrations [43]. To perform the following analysis, several TNEP models were trained using `GPUMD` to predict BECs based on data generated by density functional perturbation theory (DFPT). While DFT calculates the ground-state properties, DFPT evaluates the system's response to small perturbations, such as an applied electric field. This enables the calculation of properties such as BECs.

4.2.1 TNEP model

The TNEP models were trained on DFPT-calculated BEC data from three different space groups of calcium titanate: perovskite ($Pnma$), RP phase ($n = 1$, $Pbca$), and RP phase ($n = 2$, $Cmc2_1$).

These structures contain 20, 28, and 24 atoms, respectively. For each structure, MD simulations were conducted to simulate heating from 0 K to 2000 K and from each MD trajectory, 100 snapshots were extracted, providing a diverse training dataset.

To evaluate model performance, the data were split into training and testing sets with six different ratios ranging from 50:50 to 95:5, using `StratifiedShuffleSplit` from `Scikit-Learn` to ensure uniform coverage across the entire temperature range [42]. Loss functions and parity plots for the models trained with 50% and 95% of the data are shown in Figure 4.14. The performance improves noticeably with a higher training fraction. It is observed that the model trained with 95% of the data demonstrates clear separation between the different atomic BEC values, in contrast to the more scattered predictions from the model trained on only 50%.

To further assess generalization, the trained models were tested on a structure not included in the training set: the RP phase with $n = 4$ ($Cmc2_1$), using a $3 \times 3 \times 3$ supercell (1188 atoms in total). A two-picosecond MD simulation at a constant temperature of 300 K was conducted, and BECs were predicted for every frame, as shown in Figure 4.15.

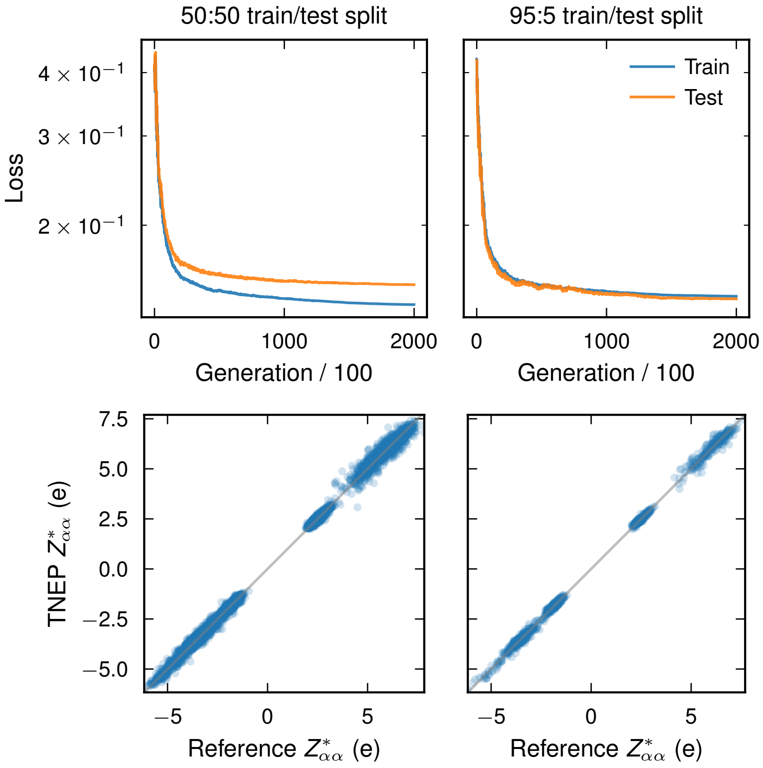

Figure 4.14: Loss functions and parity plots for TNEP models trained with 50:50 and 95:5 train:test splits.

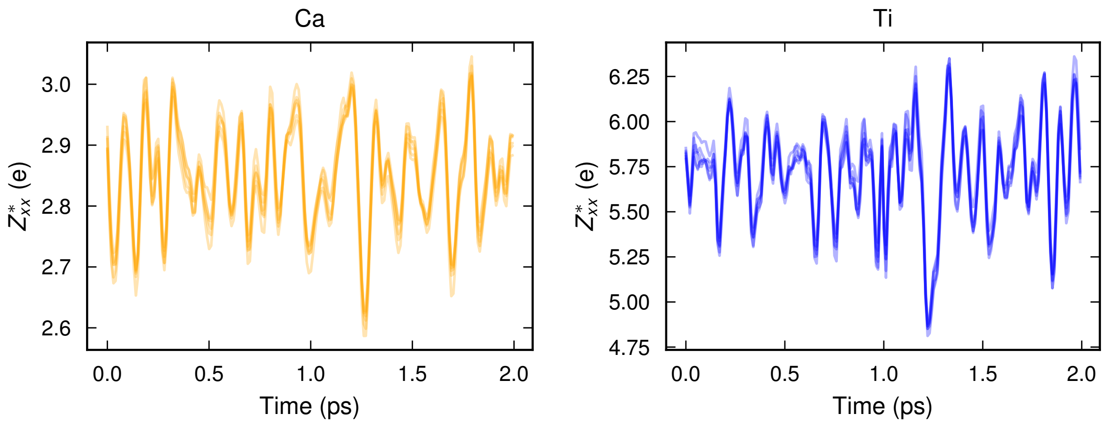

Figure 4.15: Predicted Z^*_{xx} components over time for Ca and Ti atoms during an MD simulation at constant temperature 300 K.

Only the Z^*_{xx} component is shown here, since the diagonal elements of the BEC tensors for Ca and Ti are very similar in magnitude. Since the focus is on comparing model performances, the directions of the tensor components are not the primary concern. However, for O, all diagonal components are plotted as the values vary significantly between the diagonal components. This variation is attributed to the fact that Z^*_{xx} is along the direction of the bonds.

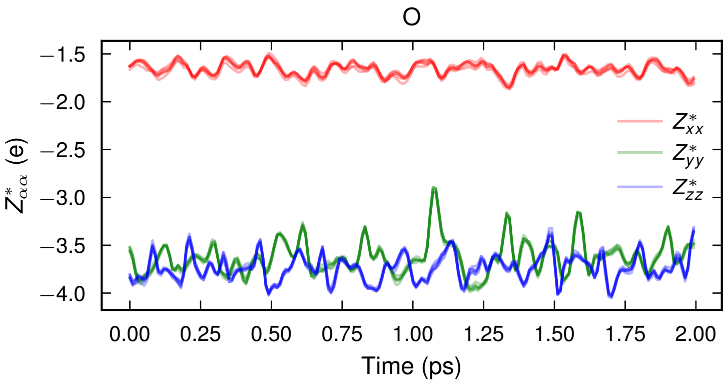

Figure 4.16: Predicted $Z^*_{\alpha\alpha}$ components over time for O atoms during an MD simulation at constant temperature 300 K.

Across all six models, the predictions are highly consistent, demonstrating a successful generalization to unseen structures.
To quantify model uncertainty, the standard deviation of the averaged diagonal BEC components (Z^*_{avg}) across all models and atom types was evaluated. This was done using the same MD heating simulations that were used to train the models. Two representative structures were chosen: the *Pnma* phase (included in training) and the RP phase (Cmc2_1 with $n = 4$), which was not included in training.

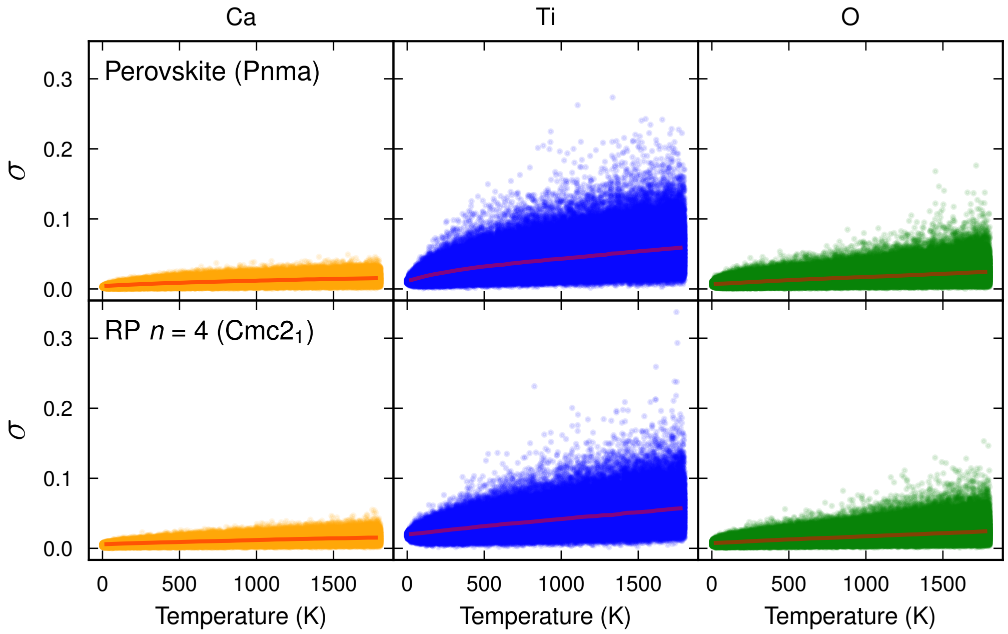

Figure 4.17: Standard deviation of the average of the diagonal elements of Z^* for each atom, further averaged over all six models.

The standard deviations remain within a reasonable range for all atom types, and both structures. The trends between the two structures are also similar, indicating good model reliability.

4.2.2 Vibrational properties

The same heating run was used to analyze the $n = 4$ RP phase ($Cmc2_1$). For each model, the diagonal elements of the BEC tensors were averaged, followed by an additional averaging across the six models. To gain insight into the electron-phonon coupling, the temperature-dependent variation in the average BEC, Z^*_{avg}, is shown in Figure 4.18.

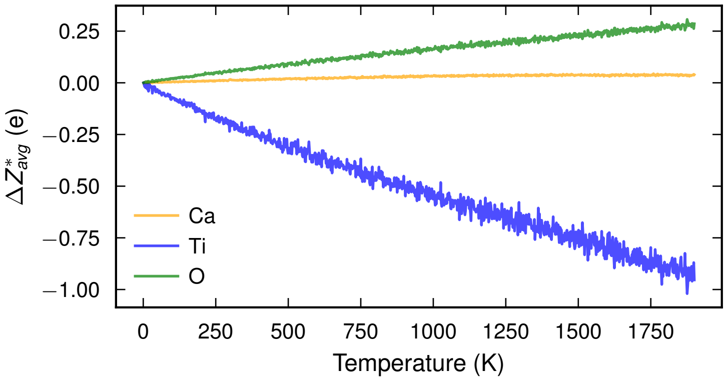

Figure 4.18: Variation of Z^*_{avg} with temperature for the three different atom types. Ti has a strong coupling to thermal vibrations, whereas Ca and O exhibit weaker coupling.

Among the atom types, Ti shows the largest change in Z^*_{avg}, about 1 e, across the temperature range, suggesting strong electron-phonon coupling. In contrast, the changes for Ca and O are more modest. Notably, Ca appears unaffected by temperature in comparison to the other elements, indicating weak coupling to thermal vibrations.

It is of particular interest how the diagonal BEC tensor varies along the stacking direction of RP phases with increasing number of layers, as visualized in Figure 3.3. This was evaluated for the relaxed $Cmc2_1$ RP phase with eight layers (336 atoms), using only the model trained on 95% of the data. The stacking direction of the structure lies along the z-axis, and corresponding atoms in each layer were grouped into bins. The average BEC for each atom type in each layer was then calculated along the z-coordinate of the structure, as shown in Figure 4.19. This analysis is motivated by the fact that edge regions are known to exhibit different physical properties compared to the bulk. In the figure, the BECs show a clear pattern along the stacking direction of the structure. Since the bulk of RP phases consists of repeated perovskite layers between edge regions, looking at the z-components of the BEC tensor, and focusing on Ca and Ti, we see that the BEC values in the bulk resemble those found in the bulk (3D) perovskites. This is illustrated in Figure 4.20.

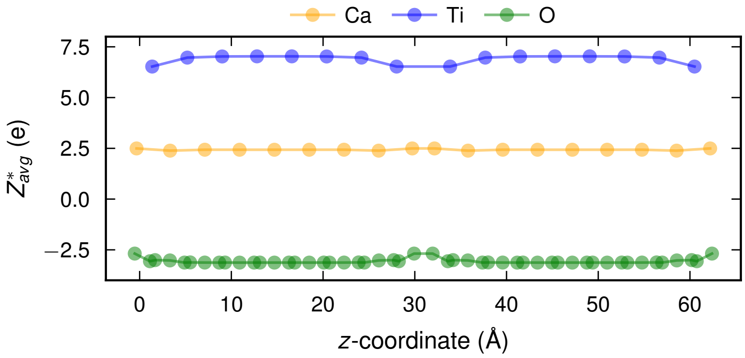

Figure 4.19: Average BEC of every atom type along the stacking direction of the $n = 8$ RP phase.

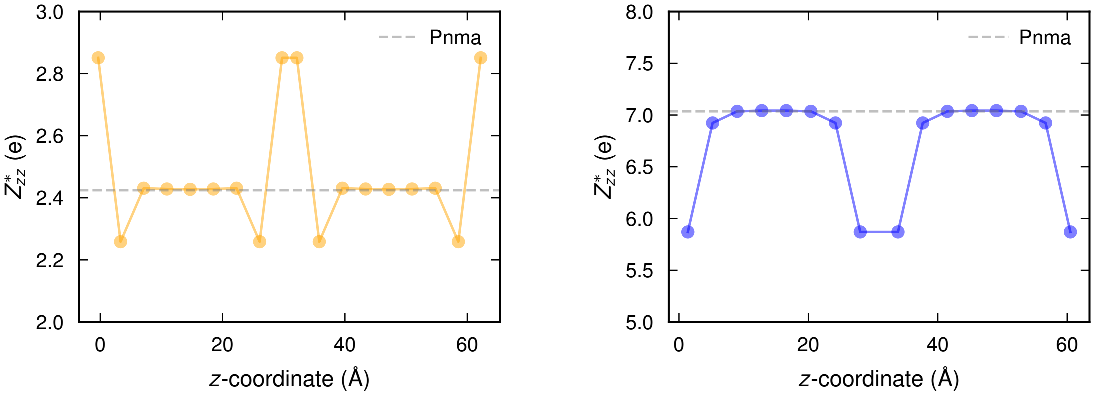

(a) Ca BECs in RP $n = 8$ compared to constant *Pnma* perovskite values.

(b) Ti BECs in RP $n = 8$ compared to constant Pnma perovskite values.

Figure 4.20: Comparison of Ca (a) and Ti (b) BECs in the RP $n = 8$ structure with BECs in the bulk *Pnma* perovskite. The BEC values are shown along the stacking direction of the RP phase, showing how they vary across the layers. Within the bulk region of the RP phase, the BECs for both Ca and Ti approach the same values as those found for the perovskite, with deviations near the edge layers.

Although the RP phase has $n = 8$ perovskite layers, only five consecutive Ca atoms along the stacking direction exhibit BECs that match the bulk perovskite value. This is due to interface effects from the rocksalt layers (AO), where the Ca atoms near the AO layers experience a different local environment. This trend is consistent with prior studies of oxide RP phases, where polarization and BECs have been shown to vary near the interfaces, and converge to bulk values deeper within the perovskite block [44]. For Ti, the Ti-O chains along the stacking direction are broken at the interface, significantly reducing the BECs by approximately 1 e. In contrast, Ca does not form directional bonds like Ti, and its BECs show a smaller, though still significant, variation of around 0.6 e. Interestingly, the BEC for Ca slightly decreases just before the interface, then increases again at the interface. This is opposite to the trend seen for Ti, where the BECs are suppressed at the edge. This behavior for Ca might be related to local structural distortions near the interface, such as octahedral tilting, which can modify the environment and charge response. Nevertheless, the Ca atoms clearly resemble the perovskite bulk values of the BEC in the central layers.

The ability of the model to reproduce the expected coordinate variation in BECs, including the perovskite values in the inner layers indicate that the model is capable of predicting real scenario BECs well beyond its training set.

4.3 Polarization for $Ca_3Ti_2O_7$

The predicted BEC tensors were used to analyze the polarization of the RP ($n = 2$) oxide $Ca_3Ti_2O_7$. To estimate the polarization, the linear approximation in Eq. (2.37) was applied, using atomic displacements relative to two different reference structures: the relaxed non-polar phase with space group $I4/mmm$, and the initial configuration of the polar phase with space group $Cmc2_1$. Both RP phases were constructed with 96 atoms and relaxed with the NEP model. Further, the $Cmc2_1$ structure was used in an MD simulation at 300 K in the NVT ensemble. The polarization was then computed over time using both references to assess the influence of distortions.

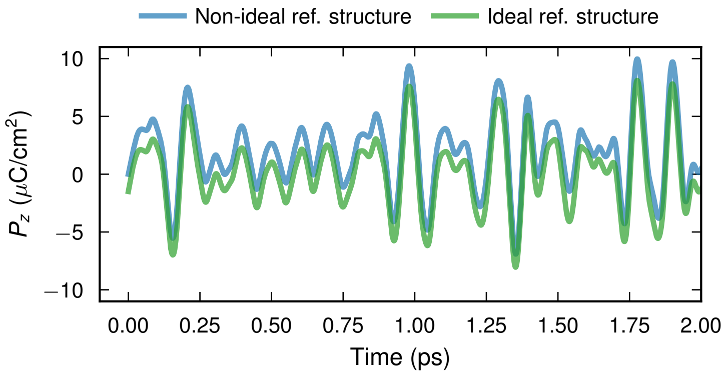

Figure 4.21: Predicted polarization over time at 300 K using two different reference structures for the atomic displacements: the relaxed $I4/mmm$ structure and the non-equilibrium $Cmc2_1$ structure obtained from the first frame of the MD simulation.

An arbitrary component of $\mathbf{P}$ was used for demonstrating the effect of the reference structure. As shown in Figure 4.21, the difference between reference structures influences the polarization minimally. To stay consistent with literature, the non-polar ideal reference structure was used for further analysis of the polarization.

The next question to address was whether using ideal or configuration-dependent BECs provide consistent polarizations. Ideal BECs refer to $Z^*_{i\mu\nu}$ tensors calculated for the ideal $I4/mmm$ reference structure, and used throughout the whole range of displacements. Configuration-dependent BECs were calculated at every frame of the MD simulation for the $Cmc2_1$ structure, and used with the corresponding

displacements with respect to the ideal reference structure. The reason for this comparison is the possibility of reduced complexity of the calculations. For large systems, the amount of BEC data increases rapidly when calculated at every frame. Since predictions are made for each atom in each frame, systems containing several thousand atoms or more generate very large BEC tensor datasets. Using only the reference structure for BEC tensors avoids this issue.
The comparison between ideal and configuration-dependent BECs is shown in Figure 4.22.

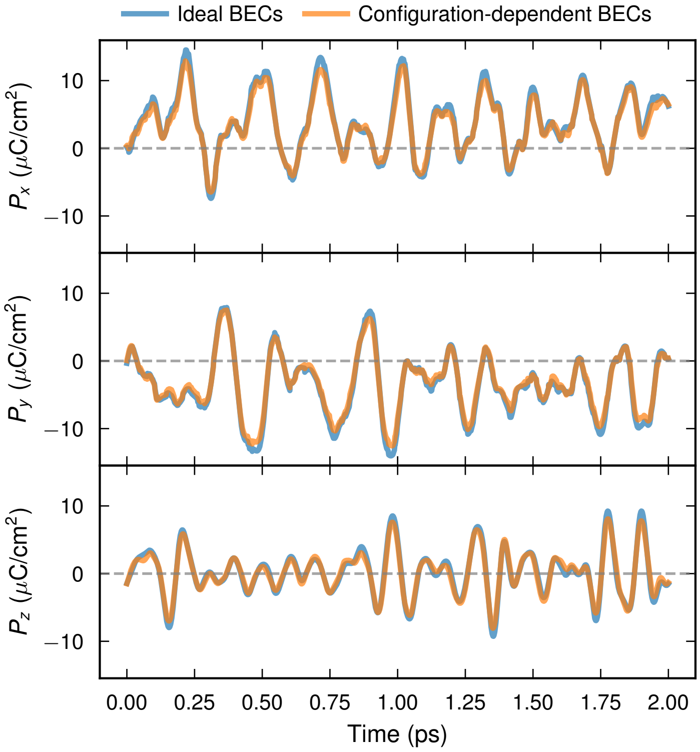

Figure 4.22: Comparison of static and configuration-dependent BECs for all polarization components. The difference is negligible, and for further analysis the ideal BECs were used.

Across all components of the polarization, the result is consistent for both ideal and configuration-dependent BECs. With this reassurance, the ideal BECs were used for continued analysis.
The following step was to compare the predicted polarization with data from DFT. During the first picosecond in the MD simulation, 20 equally distributed frames were extracted for DFT calculations. In VASP, the `LCALCPOL` command executes the evaluation of the Berry phase expressions for the electronic polarization and calculates the electronic contribution to the polarization along three reciprocal lattice vectors. The polarization is only defined modulo $fe\mathbf{R}/\Omega$, where f is the occupation factor and $\mathbf{R}$ is the lattice vector. What is interesting is the polarization changes $|\Delta\mathbf{P}| \ll |fe\mathbf{R}_1/\Omega|$ where $\mathbf{R}_1$ is the shortest lattice vector [45]. Thus, one must fix the center of reference for the Berry phase calculations, which otherwise leads to jumps proportional to the lattice vector.

This was handled in `Python` by subtracting integer multiples of the lattice vectors, shifting the values back into the central range, and removing artificial jumps. This unwrapping procedure ensures that only physically meaningful changes in polarization are retained. Unlike previous figures, which use a single TNEP model trained with 95% of the data, Figure 4.23 compares DFT polarization values with predictions from three TNEP models, all trained on the data split but initialized with different random seeds. The mean prediction is shown, with shaded regions representing ± 20 standard deviations at each time step, scaled for visual clarity.

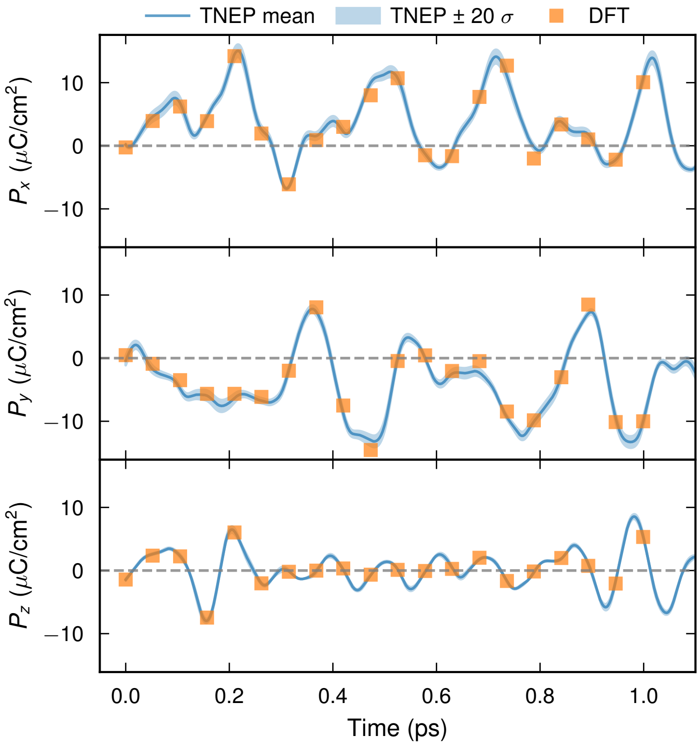

Figure 4.23: Comparison of the polarization components obtained from TNEP BECs and DFT reference data. The TNEP prediction shown is the mean over three independently trained models, with shaded regions representing the standard deviation ($\pm 20\,\sigma$). The mean polarization values for P_x, P_y, and P_z are 3.99, -4.06, and $0.18\,\mu\text{C/cm}^2$, respectively, with corresponding average standard deviations of 0.028, 0.029, and $0.009\,\mu\text{C/cm}^2$

By observing Figure 4.23, the resemblance between TNEP-predicted polarization and DFT data is clear, and support the model's reliability. The average standard deviation between models is less than $0.03\,\mu\text{C/cm}^2$ for P_x and P_y, and below $0.01\,\mu\text{C/cm}^2$ for P_z, indicating model consistency. The mean values of P_x and P_y are $\sim 4\,\mu\text{C/cm}^2$, which is consistent with the polarization at 300 K during a heating simulation of a larger system in the NpT ensemble, as will be shown later in Figure 4.28.

With the confirmation that the predicted polarization is in agreement with DFT data, a heating simulation using the NpT ensemble was performed for a larger system consisting of 49 152 atoms for the $Cmc2_1$ space group. The structure was heated from 1 K to 1500 K, and lattice parameters were extracted throughout the heating simulation to observe the phase transitions.

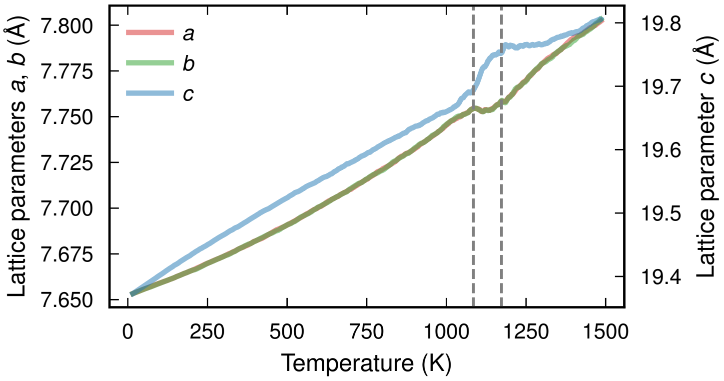

Figure 4.24: Temperature dependence of the lattice parameters. Lattice parameters a and b are plotted on the left y-axis, and parameter c is plotted on the right y-axis. Vertical dashed lines indicate inflection points in the lattice parameters, corresponding to phase transitions at $\sim 1100\,\mathrm{K}$ and $\sim 1200\,\mathrm{K}$.

Figure 4.24 reveals an initial phase transition at approximately 1100 K, and a second phase transition at approximately 1200 K. They are known to be a ferroelectric to paraelectric phase transition from polar $Cmc2_1$ to non-polar $Ccce$, and then a non-polar transition $Ccce$ to $I4/mmm$ [46, 47].
To gain further insight into the phase transitions, the angles between the respective cell vectors were extracted over the heating simulation.

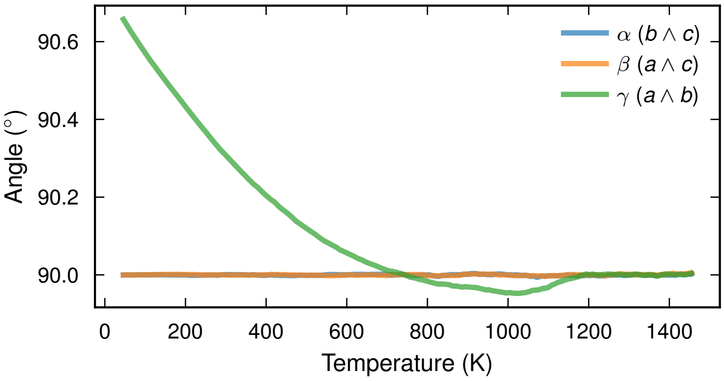

Figure 4.25: Evolution of the angles between cell vectors during heating, illustrating the phase transition. Initially, the structure is in the $Cmc2_1$ phase, characterized by a non-90° γ-angle. At $\sim 1200\,\mathrm{K}$, the structure transitions into the $I4/mmm$ phase, where all cell angles converge to 90°.

It is seen that at high temperature, the structure is in the high-symmetry $I4/mmm$ phase, whereas for lower temperature the symmetry is lowered towards the $Cmc2_1$ phase. For the polar $Cmc2_1$ phase, the γ angle is 90.7° before decreasing towards a less than 90° angle, and finally transitioning to the non-polar $I4/mmm$ phase with all right angles.

To complement this analysis, the octahedral tilt angles were extracted for all Cartesian directions over the heating simulation. In Figure 4.26, we observe out-of-phase tilting in the z-direction between $\sim 1000\,\mathrm{K}$ and $\sim 1200\,\mathrm{K}$, and the two phase transitions are clear.

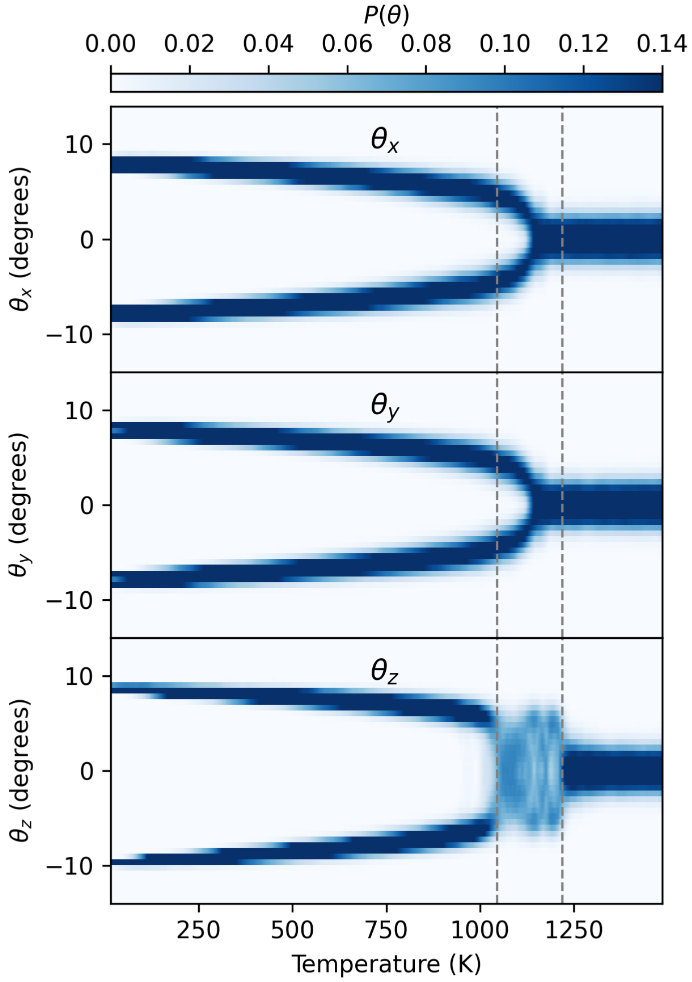

Figure 4.26: Distribution of the octahedral tilt angles as a function of temperature. The phase transitions at $\sim 1000\,\mathrm{K}$ and $\sim 1200\,\mathrm{K}$ are clear for θ_z, where we observe out-of-phase tilting.

With the phase transition behavior clarified, the next step was to investigate the temperature dependence of the polarization. When calculating displacements over a simulation using the NpT ensemble, one must be careful with movements of the cell. To obtain physically consistent atomic displacements, a frame-wise averaging was made with reference to the relaxed $Cmc2_1$ ground state structure. Each MD snapshot was aligned to this structure, and averaged over 20 frames. The displacements of these 20 frames are calculated with respect to the ground state structure and averaged, removing non-systematic motion.

Having the time averaged trajectory, the displacements in all Cartesian directions for each atom type were calculated with respect to the centrosymmetric $I4/mmm$ phase, as for previous polarization calculations.

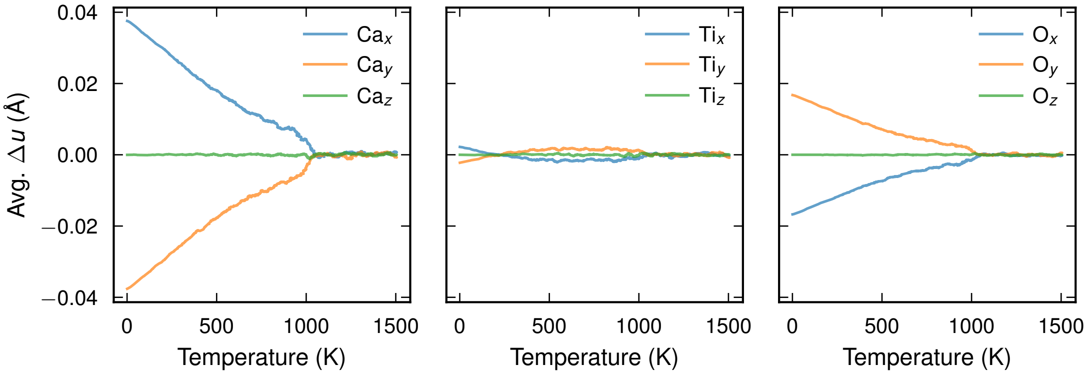

Figure 4.27: Average displacement from the reference structure over the heating run for each atom type and Cartesian direction. The displacement drastically drops around 1000 K, consistent with the structure transitioning from the polar $Cmc2_1$ phase to the non-polar $Ccce$ phase.

In the RP phase for $Ca_3Ti_2O_7$, the structure is composed of TiO_6 octahedra, where the Ti atoms sit at the centers of these octahedra and exhibit small displacements. In contrast, the oxygen atoms, positioned at the corners of the octahedra, participate in the rotation and tilting of the structure, leading to larger displacements. The Ca atoms form non-cancelling displacements due to the rotation and tilts of the octahedra, inducing hybrid improper ferroelectricity. Two of three cation layers are directed along the [110] direction and the third is anti-parallel, yielding a net polarization in the RP phase. Figure 4.27 capture this behavior, where the displacements are observed for the low-symmetry phase for calcium and oxygen. From the evolution of displacements during the heating, the phase transition to the non-polar phase is clear.

As stated, the high-symmetry phase exhibit zero polarization by symmetry, hence the sum in Eq. (2.37) for the distorted phase yields the spontaneous polarization of the ferroelectric phase. In Figure 4.28, this is clearly observed as the polarization components approach zero at the phase transition temperature, since the displacements in Figure 4.27 vanish.

The decomposed polarization reflects the transition from the ferroelectric $Cmc2_1$ to the paraelectric $I4/mmm$ structure. The polarization reaches zero at ~ 1100 K, which is consistent with experimental measurements of T_c for $Ca_3Ti_2O_7$ [48]. It has been determined that the ferroelectric to paraelectric phase transition occurs through an initial loss in octahedral tilting, which is then followed by a loss in octahedral rotation. This indicates the presence of the non-polar intermediate $Ccce$ phase. Thus, the second phase transition at higher temperature will not be reflected in the polarization response. To further observe the ferroelectric to paraelectric phase transition being reflected in the predicted polarization, the magnitude of the polarization vector was computed and compared against experimental data between ~ 300 K and ~ 1200 K from [47].

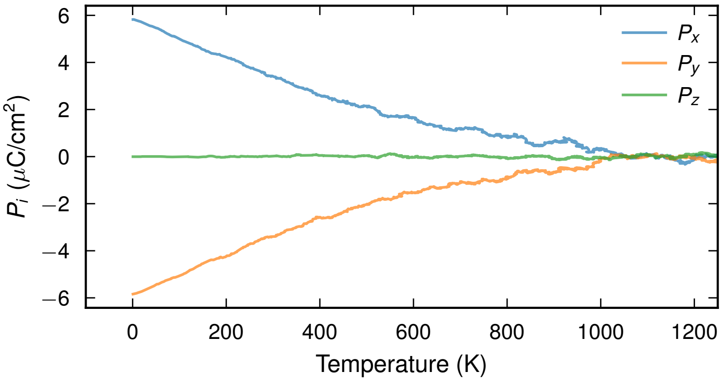

Figure 4.28: Polarization decomposed into x, y, z components over heating. The ferroelectric to paraelectric transition is observed at $\sim 1100\,\mathrm{K}$.

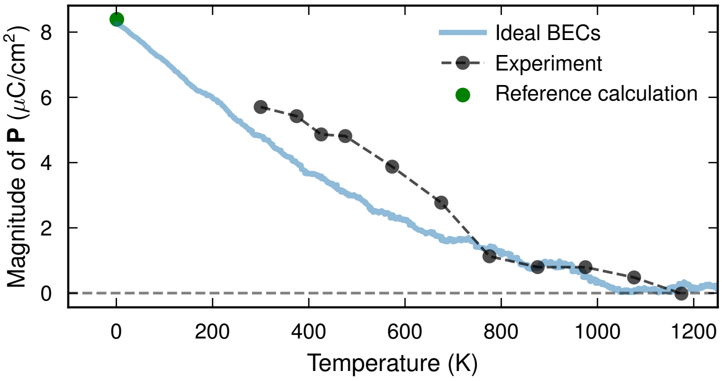

Figure 4.29: Temperature dependence of the polarization magnitude from MD compared with experimental data. The polarization shows a sharp drop at the ferroelectric to paraelectric phase transition.

A consistency check was performed by comparing the polarization magnitude calculated from the relaxed $Cmc2_1$ structure (relative to the relaxed $I4/mmm$ reference) with the polarization obtained from the first frame of the MD trajectory. The agreement confirms that the polarization is captured accurately, and that no artificial displacements are introduced at the start of the simulation. At this state, the polarization is calculated to be around $8\,\mu C/\mathrm{cm}^2$, a value which has been confirmed in previous studies [32]. By observing Figure 4.29, it is clear that the experimental data follow Landau phase transition theory up to the temperature $T_d \sim 800\,\mathrm{K}$, with polarization scaling as $P \sim (T_d - T)^{0.5}$. In contrast, the model prediction does not follow the expected Landau-like behavior below T_d, although it aligns reasonably well with the experimental trend above T_d.

The deviation from Landau phase transition theory is already indicated in Figure 4.27, where the atomic displacement pattern shift around $\sim 800\,\mathrm{K}$ from a linear, slowly declining behavior, to a sharper drop which resembles the expected Landau behavior with a critical exponent $\beta < 1$. This transition in the displacement behavior indicates that the polarization is unlikely to follow the $(T_c - T)^\beta$ dependence in

the regime below T_d.
To quantify the temperature dependence of the polarization near the phase transition, the polarization was fit using the `curve_fit` routine from `SciPy` in the temperature range $T > T_d$, according to $P(T) \sim (T_c - T)^\beta$ [49].
The fit yields a Curie temperature of $T_c \sim 1041\,\mathrm{K}$ and a critical exponent $\beta = 0.559$, consistent with classical mean-field behavior in Landau theory. This result contrasts with the experimental data, where polarization follows Landau theory with $\beta = 0.5$ below T_d, whereas a smaller exponent $\beta = 0.13$ is reported above T_d and a Curie temperature of $T_c \sim 1082\,\mathrm{K}$. However, the experimental data does not show a non-polar intermediate phase as expected, whereas the model shows a clear drop in polarization at the expected ferroelectric to paraelectric phase transition.

5

Conclusion

In this work, different approaches to modeling electron-phonon coupling were explored for two perovskite systems: $CsPbBr_3$ and $CaTiO_3$, and for the oxide perovskite, including RP phases. The overall conclusion is that it is relatively straightforward to build useful models for electron-phonon coupling, even with simple methods. In the case of the halide perovskite, the model is not perfect, but gives adequate results and can be used to gain insight into the relationship between mode behavior and fluctuations in the band edges. In this case, extending the dataset would likely improve model performance further and could be a direction for future work. Though the fluctuations in the VBM are rapid, more complex relationships between ε_{VBM} and Q_n would likely yield a better fit. Still, this work shows that simplified models are sufficient to provide meaningful insights into electron-phonon interactions. Future work could also explore how mode distortions affect specific **k**-points, including flat band regions, offering a deeper understanding of local changes in the electronic structure of perovskites.

For $CsPbBr_3$, the focus was on modeling VBM fluctuations during molecular dynamics simulations at constant temperature in the cubic phase. Using squared phonon mode coordinates as features, it was possible to capture the rapid VBM fluctuations reasonably well. Feature selection showed that only a subset of modes contributed meaningfully the VBM variation, and the analysis identified octahedral tilt modes as the most influential. Displacements along these modes were found to widen the band gap compared to the undistorted structure.

In the oxide part of the study, TNEP models were trained on BECs. The models remained consistent when applied to unseen RP phases, showing only small differences in prediction uncertainty compared to structures included in training. The model's performance with a 50:50 split was slightly worse in terms of loss and parity, as shown in Figure 4.14, but the test predictions during MD at 300 K remained qualitatively similar, as seen in Figure 4.15. Importantly, the model with a 95:5 split captured the suppression of BECs at Ti–O chain break points at the interfaces, a known effect reported in previous work. It also reproduced intermediate BEC values in the bulk of the unseen RP phase, consistent with the expected behavior when moving through layered RP structures.

Temperature effects were also well captured with the TNEP model. Titanium atoms showed significantly stronger temperature-dependent charges than calcium or oxygen. The model predicted polarization trends in $Ca_3Ti_2O_7$ accurately, including the loss of polarization during the ferroelectric to paraelectric phase transition from $Cmc2_1$ to the intermediate $Ccce$ phase. It was also confirmed that using ideal versus configuration-dependent BEC methods and choice of reference structure (relaxed

$I4/mmm$ vs. first MD frame) only have minor influence on polarization predictions. Finally, based on the drop in atomic displacements and polarization, the Curie temperature for $Ca_3Ti_2O_7$ was identified to be around 1041 K, consistent with the observed phase transition from $Cmc2_1$ to $Ccce$. A second transition to the high-symmetry $I4/mmm$ phase occurred at 1200 K. Near the Curie temperature, the polarization was found to follow a temperature dependence consistent with Landau theory above $\sim 800\,\mathrm{K}$, yielding a critical exponent of $\beta \approx 0.56$.

To this end, this work shows that even simple models can provide useful insights into electron-phonon coupling, both in terms of mode contributions to band edge fluctuations and the temperature dependence of polarization. These approaches can be extended to larger-scale simulations, enabling more efficient exploration of phase behavior and electronic properties across a wide range of structures.

Bibliography

[1] A. K. Jena, A. Kulkarni, and T. Miyasaka, "Halide perovskite photovoltaics: Background, status, and future prospects," *Chemical Reviews*, vol. 119, no. 5, pp. 3036–3103, 2019. DOI: `10.1021/acs.chemrev.8b00539`.

[2] J. You, L. Meng, T.-B. Song, *et al.*, "Improved air stability of perovskite solar cells via solution-processed metal oxide transport layers," *Nature Nanotechnology*, vol. 11, pp. 75–81, 2016. DOI: `10.1038/nnano.2015.230`.

[3] X. Li, M. Ibrahim Dar, C. Yi, *et al.*, "Improved performance and stability of perovskite solar cells by crystal crosslinking with alkylphosphonic acid ω-ammonium chlorides," *Nature Chemistry*, vol. 7, pp. 703–711, 2015. DOI: `10.1038/nchem.2324`.

[4] J. Wiktor, U. Rothlisberger, and A. Pasquarello, "Predictive determination of band gaps of inorganic halide perovskites," *The Journal of Physical Chemistry Letters*, vol. 8, no. 22, pp. 5507–5512, 2017. DOI: `10.1021/acs.jpclett.7b02648`.

[5] X. Zhu and D. A. Egger, *The effect of overdamped phonons on the fundamental band gap of perovskites*, 2024. arXiv: `2406.05201 [cond-mat.mtrl-sci]`. [Online]. Available: `https://arxiv.org/abs/2406.05201`.

[6] I. Tsidilkovski, "Chapter 1 - methods of calculating band structure," in *Band Structure of Semiconductors*, ser. International Series in the Science of the Solid State, I. Tsidilkovski, Ed., vol. 19, Pergamon, 1982, pp. 11–76, ISBN: 978-0-08-021657-7. DOI: `10.1016/B978-0-08-021657-7.50007-8`.

[7] M. Nisoli, "Band structure of semiconductors," in *Semiconductor Laser Photonics.* Cambridge University Press, 2022, pp. 1–39.

[8] P. Hohenberg and W. Kohn, "Inhomogeneous electron gas," *Phys. Rev.*, vol. 136, B864–B871, 3B Nov. 1964. DOI: `10.1103/PhysRev.136.B864`.

[9] F. Giustino, *Materials Modelling Using Density Functional Theory: Properties and Predictions.* Oxford University Press, 2014, ISBN: 978-0-19-966243-2.

[10] F. Zahariev, S. S. Leang, and M. S. Gordon, "Functional derivatives of meta-generalized gradient approximation (meta-gga) type exchange-correlation density functionals," *The Journal of Chemical Physics*, vol. 138, no. 24, p. 244 108, Jun. 2013, ISSN: 0021-9606. DOI: `10.1063/1.4811270`.

[11] W. Nolting and W. D. Brewer, *Fundamentals of Many-body Physics: Principles and Methods*, 1st ed. Springer-Verlag Berlin Heidelberg, 2009, Published online: 29 September 2009, ISBN: 978-3-540-71931-1. DOI: `10.1007/978-3-540-71931-1`.

[12] P. Zhong, D. Kim, D. S. King, and B. Cheng, *Machine learning interatomic potential can infer electrical response*, 2025. arXiv: `2504.05169`

`[cond-mat.mtrl-sci]`. [Online]. Available: `https://arxiv.org/abs/2504.05169`.

[13] C. Carbogno *et al.*, *Polarisation, born effective charges, and topological invariants via a berry-phase approach*, 2025. arXiv: `2501.02550 [cond-mat.mtrl-sci]`. [Online]. Available: `https://arxiv.org/abs/2501.02550`.

[14] K. M. Rabe and P. Ghosez, "First-principles studies of ferroelectricoxides," in *Physics of Ferroelectrics: A Modern Perspective.* Berlin, Heidelberg: Springer Berlin Heidelberg, 2007, pp. 117–174, ISBN: 978-3-540-34591-6. DOI: `10.1007/978-3-540-34591-6_4`.

[15] S. Falletta *et al.*, *Unified differentiable learning of electric response*, 2024. arXiv: `2403.17207 [cond-mat.mtrl-sci]`. [Online]. Available: `https://arxiv.org/abs/2403.17207`.

[16] P. Umari and A. Pasquarello, "Infrared and raman spectra of disordered materials from first principles," *Diamond and Related Materials*, vol. 14, no. 8, pp. 1255–1261, 2005, SMAC '04 Conference Proceeding S.I., ISSN: 0925-9635. DOI: `10.1016/j.diamond.2004.12.007`.

[17] X. Gonze and C. Lee, "Dynamical matrices, born effective charges, dielectric permittivity tensors, and interatomic force constants from density-functional perturbation theory," *Phys. Rev. B*, vol. 55, pp. 10 355–10 368, 16 Apr. 1997. DOI: `10.1103/PhysRevB.55.10355`.

[18] J. Meller, "Molecular dynamics," in *eLS*. John Wiley & Sons, Ltd, 2001, ISBN: 9780470015902. DOI: `10.1038/npg.els.0003048`.

[19] T. Zheng, W. Gao, and C. Wang, *Learning large-time-step molecular dynamics with graph neural networks*, 2021. arXiv: `2111.15176 [physics.comp-ph]`. [Online]. Available: `https://arxiv.org/abs/2111.15176`.

[20] G. Bussi, D. Donadio, and M. Parrinello, "Canonical sampling through velocity rescaling," *The Journal of Chemical Physics*, vol. 126, no. 1, p. 014 101, Jan. 2007, ISSN: 0021-9606. DOI: `10.1063/1.2408420`.

[21] H. J. C. Berendsen, J. P. M. Postma, W. F. van Gunsteren, A. DiNola, and J. R. Haak, "Molecular dynamics with coupling to an external bath," *The Journal of Chemical Physics*, vol. 81, no. 8, pp. 3684–3690, Oct. 1984, ISSN: 0021-9606. DOI: `10.1063/1.448118`.

[22] J. Brorsson *et al.*, "Efficient calculation of the lattice thermal conductivity by atomistic simulations with ab initio accuracy," *Advanced Theory and Simulations*, vol. 5, no. 2, p. 2 100 217, 2022. DOI: `10.1002/adts.202100217`.

[23] N. Xu *et al.*, "Tensorial properties via the neuroevolution potential framework: Fast simulation of infrared and raman spectra," *Journal of Chemical Theory and Computation*, vol. 20, no. 8, pp. 3273–3284, 2024. DOI: `10.1021/acs.jctc.3c01343`.

[24] E. Fransson, J. Wiktor, and P. Erhart, "Phase transitions in inorganic halide perovskites from machine-learned potentials," *The Journal of Physical Chemistry C*, vol. 127, no. 28, pp. 13 773–13 781, 2023. DOI: `10.1021/acs.jpcc.3c01542`.

[25] T. Das, G. Di Liberto, and G. Pacchioni, "Density functional theory estimate of halide perovskite band gap: When spin orbit coupling helps," *The Journal*

of Physical Chemistry C, vol. 126, no. 4, pp. 2184–2198, 2022. DOI: `10.1021/acs.jpcc.1c09594`.

[26] R. X. Yang, J. M. Skelton, E. L. da Silva, J. M. Frost, and A. Walsh, "Spontaneous octahedral tilting in the cubic inorganic cesium halide perovskites cssnx3 and cspbx3 (x = f, cl, br, i)," *The Journal of Physical Chemistry Letters*, vol. 8, no. 19, pp. 4720–4726, 2017. DOI: `10.1021/acs.jpclett.7b02423`.

[27] R. X. Yang, J. M. Skelton, E. L. da Silva, J. M. Frost, and A. Walsh, "Assessment of dynamic structural instabilities across 24 cubic inorganic halide perovskites," *The Journal of Chemical Physics*, vol. 152, no. 2, p. 024 703, Jan. 2020, ISSN: 0021-9606. DOI: `10.1063/1.5131575`.

[28] Z. Li, M. Yang, J.-S. Park, S.-H. Wei, J. J. Berry, and K. Zhu, "Stabilizing perovskite structures by tuning tolerance factor: Formation of formamidinium and cesium lead iodide solid-state alloys," *Chemistry of Materials*, vol. 28, no. 1, pp. 284–292, 2016. DOI: `10.1021/acs.chemmater.5b04107`.

[29] Q. Fu, M. Chen, Q. Li, H. Liu, R. Wang, and Y. Liu, "Selenophene-based 2d ruddlesden-popper perovskite solar cells with an efficiency exceeding 19%," *Journal of the American Chemical Society*, vol. 145, no. 39, pp. 21 687–21 695, 2023. DOI: `10.1021/jacs.3c08604`.

[30] J. R. Kim, J. Jang, K. J. Go, *et al.*, "Stabilizing hidden room-temperature ferroelectricity via a metastable atomic distortion pattern," *Nature Communications*, vol. 11, p. 4944, 2020. DOI: `10.1038/s41467-020-18741-w`.

[31] K.-E. Hasin, N. Pokhrel, and E. A. Nowadnick, "Piezoelectricity in n = 2 ruddlesden–popper ferroelectric oxides," *Chemistry of Materials*, vol. 36, no. 15, pp. 7552–7560, 2024. DOI: `10.1021/acs.chemmater.4c01534`.

[32] B. H. Zhang, D. Xu, R. Z. Guo, L. Liu, X. Q. Liu, and X. M. Chen, "Hybrid improper ferroelectricity and phase transition behavior of li2nd2ti3o10 ceramics with a-site ordered triple-layer ruddlesden-popper structure," *Journal of Materiomics*, vol. 10, no. 1, pp. 145–153, 2024, ISSN: 2352-8478. DOI: `10.1016/j.jmat.2023.04.012`.

[33] S. Guo *et al.*, "Exciton engineering of 2d ruddlesden–popper perovskites by synergistically tuning the intra and interlayer structures," *Nature Communications*, vol. 15, no. 1, p. 3001, 2024. DOI: `10.1038/s41467-024-47225-4`.

[34] D. Lee and H. N. Lee, "Controlling oxygen mobility in ruddlesden–popper oxides," *Materials*, vol. 10, no. 4, 2017, ISSN: 1996-1944. DOI: `10.3390/ma10040368`.

[35] E. Lindgren *et al.*, "Calorine: A python package for constructing and sampling neuroevolution potential models," *Journal of Open Source Software*, vol. 9, no. 95, p. 6264, 2024. DOI: `10.21105/joss.06264`.

[36] Z. Fan, W. Chen, V. Vierimaa, and A. Harju, "Efficient molecular dynamics simulations with many-body potentials on graphics processing units," *Computer Physics Communications*, vol. 218, pp. 10–16, 2017, ISSN: 0010-4655. DOI: `10.1016/j.cpc.2017.05.003`.

[37] A. Hjorth Larsen *et al.*, "The atomic simulation environment—a python library for working with atoms," *Journal of Physics: Condensed Matter*, vol. 29, no. 27, p. 273 002, Jun. 2017. DOI: `10.1088/1361-648X/aa680e`.

[38] Z. Fan *et al.*, "Neuroevolution machine learning potentials: Combining high accuracy and low cost in atomistic simulations and application to heat transport," *Phys. Rev. B*, vol. 104, p. 104 309, 10 Sep. 2021. DOI: `10.1103/PhysRevB.104.104309`.

[39] A. Togo, "First-principles phonon calculations with phonopy and phono3py," *J. Phys. Soc. Jpn.*, vol. 92, no. 1, p. 012 001, 2023. DOI: `10.7566/JPSJ.92.012001`.

[40] F. Eriksson, E. Fransson, and P. Erhart, "The hiphive package for the extraction of high-order force constants by machine learning," *Advanced Theory and Simulations*, vol. 2, no. 5, p. 1 800 184, 2019. DOI: `10.1002/adts.201800184`.

[41] E. Fransson, F. Eriksson, and P. Erhart, "Efficient construction of linear models in materials modeling and applications to force constant expansions," *npj Computational Materials*, vol. 6, no. 1, p. 135, 2020, ISSN: 2057-3960. DOI: `10.1038/s41524-020-00404-5`.

[42] F. Pedregosa *et al.*, "Scikit-learn: Machine learning in python," *J. Mach. Learn. Res.*, vol. 12, no. null, pp. 2825–2830, Nov. 2011, ISSN: 1532-4435.

[43] G. Marchese, F. Macheda, L. Binci, M. Calandra, P. Barone, and F. Mauri, "Born effective charges and vibrational spectra in superconducting and bad conducting metals," *Nature Physics*, vol. 20, no. 1, pp. 88–94, Oct. 2023, ISSN: 1745-2481. DOI: `10.1038/s41567-023-02203-3`.

[44] N. Benedek, C. Elsässer, and M. Finnis, "First principles investigation of polarisation at interfaces in multilayered strontium titanate," *Journal of Physics: Conference Series*, vol. 94, p. 012 005, Feb. 2008. DOI: `10.1088/1742-6596/94/1/012005`.

[45] R. D. King-Smith and D. Vanderbilt, "Theory of polarization of crystalline solids," *Phys. Rev. B*, vol. 47, pp. 1651–1654, 3 Jan. 1993. DOI: `10.1103/PhysRevB.47.1651`.

[46] F. Pomiro *et al.*, "From first- to second-order phase transitions in hybrid improper ferroelectrics through entropy stabilization," *Phys. Rev. B*, vol. 102, p. 014 101, 1 Jul. 2020. DOI: `10.1103/PhysRevB.102.014101`.

[47] J. Kong *et al.*, "Scaling behavior of order parameters for the hybrid improper ferroelectric $(\mathrm{Ca},\mathrm{Sr})_3\mathrm{Ti}_2\mathrm{O}_7$," *Phys. Rev. B*, vol. 107, p. 224 103, 22 Jun. 2023. DOI: `10.1103/PhysRevB.107.224103`.

[48] X. Q. Liu *et al.*, "Hybrid improper ferroelectricity in ruddlesden-popper ca3(ti,mn)2o7 ceramics," *Applied Physics Letters*, vol. 106, no. 20, p. 202 903, May 2015, ISSN: 0003-6951. DOI: `10.1063/1.4921624`.

[49] P. Virtanen *et al.*, "SciPy 1.0: Fundamental Algorithms for Scientific Computing in Python," *Nature Methods*, vol. 17, pp. 261–272, 2020. DOI: `10.1038/s41592-019-0686-2`.

DEPARTMENT OF PHYSICS
CHALMERS UNIVERSITY OF TECHNOLOGY
Gothenburg, Sweden
www.chalmers.se